

## Article

# Characterization of Ni-Phases and Their Transformations in Fluid Catalytic Cracking (FCC) Catalysts: Comparison of Conventional Versus Boron-Based Ni-Passivation

Ioannis D. Charisteidis <sup>1</sup>, Pantelis N. Trikalitis <sup>2</sup>, Konstantinos S. Triantafyllidis <sup>1,\*</sup>, Vasileios Komvokis <sup>3,\*</sup> and Bilge Yilmaz <sup>3,\*</sup>

<sup>1</sup> Department of Chemistry, Aristotle University of Thessaloniki, 54124 Thessaloniki, Greece

<sup>2</sup> Department of Chemistry, University of Crete, Voutes, 71003 Heraklion, Greece

<sup>3</sup> BASF Corporation, 25 Middlesex/Essex Turnpike, Iselin, NJ 08830, USA

\* Correspondence: ktrianta@chem.auth.gr (K.S.T.); vasileios.komvokis@basf.com (V.K.); bilge.yilmaz@basf.com (B.Y.)

**Abstract:** Fluid Catalytic Cracking (FCC) has traditionally been a key refining process in generating transportation fuels. Recently, the focus on FCC has been further intensified as it plays an increasingly important role in the generation of key building blocks for the petrochemical industry. Nickel is considered as one of the most challenging contaminants in FCC and originates from Ni-containing compounds in petroleum fractions, not only during unit operation but also in handling of the equilibrium and spent catalysts. Despite this critical role it plays throughout the complete lifecycle of an FCC catalyst, the nature of Ni is not yet well understood at various stages of its journey after depositing on the catalyst surface. The main objective of this contribution is the qualitative and quantitative identification of the various possible phases of Ni that are usually present in an equilibrium FCC catalyst (Ecat). A series of conventional and advanced analytical techniques have been employed, including XRF, ICP-AES, PXRD, FT-IR, UV-Vis-NIR, SEM-EDS, TEM/HRTEM and STEM/EXDS, XPS, RAMAN and TPR-H<sub>2</sub>, on prototype Ni-impregnated SiO<sub>2</sub>, Al<sub>2</sub>O<sub>3</sub> and USY zeolite samples, Ni-impregnated and lab-deactivated FCC samples, and equilibrium FCC catalysts obtained from different refineries. Detailed analysis of the obtained results on the basis of background information, showed the strengths and weaknesses of the various methods. It was shown that powder x-ray diffraction (pxrd) can be effectively used for the quantitative determination of the NiO (bunsenite) phase at levels representative of equilibrium FCC catalysts. A comparison of conventional versus boron-based Ni-passivation is presented. It was shown that catalysts from boron-based technology (BBT) can keep Ni at a less-reducible state, effectively hindering its deleterious role in FCC operations.

**Citation:** Charisteidis, I.D.; Trikalitis, P.N.; Triantafyllidis, K.S.; Komvokis, V.; Yilmaz, B. Characterization of Ni-Phases and Their Transformations in Fluid Catalytic Cracking (FCC) Catalysts: Comparison of Conventional Versus Boron-Based Ni-Passivation. *Catalysts* **2023**, *14*, 3.

<https://doi.org/10.3390/catal13010003>

Academic Editor: Roman Bulánek

Received: 19 October 2022

Revised: 2 December 2022

Accepted: 9 December 2022

Published: 20 December 2022



**Copyright:** © 2022 by the authors. Licensee MDPI, Basel, Switzerland. This article is an open access article distributed under the terms and conditions of the Creative Commons Attribution (CC BY) license (<https://creativecommons.org/licenses/by/4.0/>).

**Keywords:** FCC; equilibrium catalysts; nickel poisoning and passivation; boron based technology

## 1. Introduction

For many decades Fluid Catalytic Cracking (FCC) has been providing the majority of gasoline consumed throughout the world in addition to other important transportation fuels. Its importance in providing key petrochemical feedstocks has also been rapidly increasing, which has led to renewed interest in this central refining process [1,2]. Through technological advancements, refineries turn toward opportunity crudes to be more competitive. Thus, in recent history, the global trend has been continually towards more contaminated feedstocks, significantly increasing the importance of understanding and mitigating the negative effects of contaminants that come with these heavier crudes [3,4]. Today, the importance of nickel as one of the most challenging contaminant metals on FCC catalysts has been thoroughly acknowledged [5–8]; however, even though there have

been significant developments in the mitigation of its deleterious effects, a methodical and holistic study on the nature of Ni at various stages of its lifecycle after depositing on the catalyst surface has not been available. The accumulation of Ni on the FCC particles needs to be controlled and accurately monitored for two main reasons: first, their effects on the catalyst performance as a result of the changes in product yield distribution due to their high propensity for catalyzing unwanted side reactions; and second, the necessity for low-cost and environment-friendly use or disposal of the spent FCC catalyst (i.e., recovery of metals, use as additive in the cement industry, or disposal as non-toxic waste material in landfills). With regard to the first reason, the possible reduction of NiO to Ni(0) within the riser reactor may have undesired effects on valuable gasoline and LPG yields and, most importantly, may enhance hydrogen and coke formation by promoting dehydrogenation reactions. On the other hand, if Ni exists as bulk crystalline NiO, then depending on its content, the spent FCC catalyst may be classified as “hazardous waste” with all the associated economic and environmental consequences; the lower limit in the case of NiO is 1000 ppm (0.1 wt.%) for the European Union (ECHA) [5,9,10]. Even after its use at a given refinery, equilibrium/spent catalysts (Ecat) can be used in other refineries and FCC units or other industrial applications, which further increases the importance of the European Health and Safety (EHS) classification for its proper handling throughout its complete lifecycle [11–13].

The addition of antimony (Sb) compounds or ultra-fine particles in the gas-oil feed as Ni passivators has been established as an efficient method to limit the dehydrogenation activity of metallic Ni by forming stable Sb-Ni alloys on the FCC catalyst [6,7]. However, it is known that passivation through Sb usage in the FCC unit has an inherent limit, and beyond a certain point, the introduction of additional Sb does not bring further benefit. Moreover, in addition to the increased NO<sub>x</sub> emissions and increased bottom fouling induced by Sb addition, there are also operational limitations for this passivation method. EHS concerns around antimony are also defining the Sb usage strategies of refineries; in some countries local regulations and sensitivities lead to avoidance of Sb usage completely, and for some refineries that use Sb, there are guidelines/protocols in place to stop its addition/use for a significant period (typically a week or more) before any maintenance/planned-shutdown, whereas unplanned shutdowns constitute another risk.

In terms of catalyst-based strategies for Ni passivation, taking advantage of the tendency of Ni to react with Al<sub>2</sub>O<sub>3</sub> to form bulk NiAl<sub>2</sub>O<sub>4</sub> or Ni<sub>x</sub>Al<sub>y</sub>O<sub>z</sub> spinel-like phases, the utilization of aluminas in the matrix of the FCC particles is considered the most common approach for trapping Ni [5,6,8]. In order to overcome the low mobility of Ni within the FCC catalyst and its tendency to accumulate in the periphery of the particles, tailored catalyst manufacture technologies have been developed that optimize the spatial distribution of the specialty alumina so as to favor Ni trapping in the outer parts of the particle [14]. Still, for Ni contents over ca. 1000 ppm NiO, antimony is utilized in combination with the alumina-based trapping technologies in catalyst design. Bulk NiAl<sub>2</sub>O<sub>4</sub> spinel or Ni<sub>x</sub>Al<sub>2</sub>O<sub>3+x</sub> phases are more stable in terms of reducibility compared with NiO, thus inhibiting formation of metallic Ni and its detrimental dehydrogenation activity. To this end, the formation of Ni<sub>x</sub>Al<sub>2</sub>O<sub>3+x</sub> dispersed spinel-like phases would be more advantageous compared with bulk NiAl<sub>2</sub>O<sub>4</sub>, which may also be classified as carcinogenic. More recently, a new approach for metal passivation, boron-based technology (BBT), has been developed which exploits the mobility of boron species (B) under FCC conditions, achieving a high degree of Ni passivation and significant reductions in hydrogen and delta coke, as has been successfully demonstrated in refinery operations [6,15]. Recent spectroscopic studies including DRIFTS and TPR analyses have shown that with BBT, the reducibility of nickel is hindered, which maintains it essentially at a relatively more passive state for undesirable dehydrogenation reactions.

Considering the importance of understanding and mitigating the negative effects of nickel in FCC, a detailed quantitative and qualitative characterization of the Ni phases in the spent FCC catalysts is necessary. Although a few studies in the past have dealt with

this issue [5,8,16,17], more systematic work is still required for the accurate determination of Ni and its phases, as well as its interaction with various FCC catalyst ingredients and building blocks [7,14].

The experimental and research approach of this contribution is based on two directions: (a) the preparation and advanced characterization of prototype formulations based on nickel supported on different substrates existing in the FCC particle; and (b) the detailed characterization of spent FCC particles (taken from refineries), as well as FCC catalysts that are Ni-loaded and deactivated under laboratory conditions. The capabilities and limitations of the various characterization techniques are outlined, and the combination of the obtained data enables a better understanding of the formation and nature of the various Ni phases, even for the low Ni levels of a spent FCC catalyst [15]. Furthermore, the potential of boron-based technology (BBT) in retaining Ni in a less-reducible state, thus limiting its negative role in FCC operation, is further explored.

## 2. Materials and Methods

### 2.1. Catalyst Samples

The identification of the various Ni phases was studied on three types of substrates: (a) pure ingredients of an FCC particle, i.e.,  $\text{SiO}_2$ ,  $\text{Al}_2\text{O}_3$ , and USY zeolite; (b) lab-prepared FCC catalysts loaded with Ni; and (c) FCC equilibrium catalysts (also known as Ecats) from various refineries.

For the pure ingredient samples, nickel (Ni) was loaded on the support via the classical incipient wetness method (dry impregnation) at various levels, i.e., 150 to 200,000 ppm Ni. The supports used were  $\text{SiO}_2$  (Silica Gel 60, Panreac, 40  $< \text{dp} < 63 \mu\text{m}$ ),  $\gamma\text{-Al}_2\text{O}_3$  (Engelhard 3992, 45  $< \text{dp} < 180 \mu\text{m}$ ), and USY zeolite (CBV-712, Si/Al~6, Zeolyst, after calcination at 550 °C for 3 hrs to convert the ammonium to proton form). All supports prior to impregnation were dried in air overnight at 100 °C.

Three variations of the impregnation procedure, regarding the type of Ni precursor compound and solvent, were applied for the Ni/ $\text{SiO}_2$  samples: (a) impregnation by using aqueous solutions of  $\text{Ni}(\text{NO}_3)_2 \cdot 6\text{H}_2\text{O}$  (Strem chemicals, Newburyport, MA, USA), sample series  $\text{SiO}_2\text{-Ni-X}$ , where  $x = 1\text{--}8$  and refers to the increasing content of Ni, i.e., 150, 500, 1000, 2500, 5000, 10,000, 15,000, and 20,000 ppm; (b) impregnation by using nickel octanoate  $[\text{CH}_3(\text{CH}_2)_6\text{COO}]_2\text{Ni}$  solution in mineral spirits (Ni concentration ~8%, Alfa Aesar, Haverhill, MA, USA), which was further diluted in hexane (Sigma-Aldrich, St. Louis, MO, USA), sample series  $\text{SiO}_2\text{-Ni-oc-X}$ , where  $x = 1\text{--}7$  and refers to the increasing content of Ni, i.e., 500, 1000, 2500, 5000, 10,000, 15,000, and 20,000 ppm; and (c) as in (b) but the appropriate amount of nickel octanoate solution was diluted in cyclohexane (Labskan, Bangkok, Thailand) instead of hexane, sample series  $\text{SiO}_2\text{-CH-Ni-oc-X}$ , where  $x = 1\text{--}7$  and refers to the increasing content of Ni, from 500 to 20,000 ppm, as above. In the procedures (a) and (b), the appropriate amount/volume of Ni source solution was added dropwise in the dried support material under continuous mixing. In procedure (c), the support was first impregnated until wetness with cyclohexane, followed by impregnation with the appropriate amount/volume of the nickel octanoate solution. The Ni/ $\text{Al}_2\text{O}_3$  and Ni/USY samples were prepared following procedure (c). All samples, after impregnation, were dried in air at 100 °C for 2 h, and were then calcined in air at 700 °C (heating rate 2 °C/min) for 3 h. Selected Ni/loaded samples were calcined at more severe conditions, i.e., 805 °C for 6–12 h.

The Ni-deposited FCC catalyst samples were prepared following typical preparation protocols. In brief, pre-steamed FCC catalysts (1350° F, 2 h, 100% steam) were impregnated via the Mitchell method [18], targeting at various Ni loadings, sample series BLF-CAT-x (conventional Ni-passivation without boron) and BLB-CAT-x (with Boron-based Ni-passivation functionality), where  $x = 1\text{--}4$  refers to the increasing content of Ni, i.e., 1000, 2500, 5000, and 10,000 ppm. A cyclic propylene steaming (CPS) deactivation protocol was then applied, using alternate oxidation (sulfur dioxide/steam)-reduction

(propylene/steam) cycles at ~805 °C. The CPS deactivated samples were finally calcined in a muffle furnace at 594 °C for 2 h.

The equilibrium FCC catalyst (Ecat) samples, series B-CAT-XM, obtained from different refineries, that contained Ni in the range of ca. 1300 to 5140 ppm Ni were also explored. The Ecat samples were collected at the outlet of the regenerator of the FCC units and were calcined in a muffle furnace at 594°C for 90 min before measurements.

## 2.2. Catalyst Characterization

The content of Ni in the various catalysts was determined by *Energy Dispersive X-Ray Fluorescence (EDXRF)* analysis, on a Spectro-Xepos EDXRF spectrometer with X-Lab Pro 4.0 software, a palladium (Pd) anode, at 50 W, and 50 kV. The measurements were performed in a helium atmosphere with three excitation modes: (a) compton scattering on secondary molybdenum target (energy = 35 keV; current = 1 mA); (b) X-ray beam polarized by Barkla scattering on aluminum oxide (energy = 49.2 keV; current = 0.7 mA); and (c) high intensity Bragg reflection in highly oriented pyrolytic graphite (HOPG) crystal (energy = 17.5 keV; current = 1.5 mA). A silicon drift detector with Peltier cooling with an 8 µm Moxtek Dura-Be window was used (resolution of 160 eV at 5.9 keV). The irradiation time was 300 s for every irradiation mode (15 min per sample) [19].

The identification of the various crystalline phases of Ni in the tested catalysts was conducted by *powder X-ray diffraction (PXRD)* measurements. The PXRD patterns were recorded on a PANalytical X'Pert Pro MPD system operating at 45 KV and 40 mA using CuK $\alpha$  radiation. A silicon zero-background holder was used in all cases. Typical screening scans were recorded in the range 5–90° 2θ using a 0.02° step and 3 s per step acquisition time, and slow scan runs were recorded using a 0.02° step and 13 s per step acquisition time. The patterns of all industrial FCC samples as well as of the various Ni/SiO<sub>2</sub> samples used for the calibration curves, i.e., peak area intensity of the (2 0 0) reflection of NiO (bunsenite) vs. Ni loading, were obtained under the slow scan conditions. In addition, extra-slow scan, i.e., 0.02° step and 30 s per step acquisition time was used for representative Ni/SiO<sub>2</sub> with very low Ni content i.e., 1000 and 2500 ppm.

The *Fourier-transform infrared spectroscopy (FTIR)* measurements of the catalysts were performed on a Perkin-Elmer FTIR spectrometer (PerkinElmer Corporation, Waltham, MA, USA) applying the KBr pellet method. Typically, 2 mg of the catalyst was mixed with 200 mg of KBr in an agate mortal, and the mixture was pressed under 8 tons for 30 s to form a pellet. IR absorbance spectra were obtained between 450 and 4000 cm<sup>-1</sup> at a resolution of 4 cm<sup>-1</sup> using 32 coadded scans. All spectra presented were baseline corrected and normalized.

Solid state *Diffuse reflectance UV-Vis/near IR* absorption spectra were recorded at room temperature on a Perkin Elmer LAMBDA 950 UV/Vis/NIR spectrophotometer in the wavelength range of 250–2500 nm. BaSO<sub>4</sub> powder was used as a reference (100% reflectance) and the base material on which the powder sample was coated. Reflectance data were converted to absorbance data as described elsewhere [20].

*Raman spectra* were recorded on a Raman HORIBA-XploRA system using a laser excitation line at wavelength of 532 nm in the range of 100–2000 cm<sup>-1</sup>. Samples were in the form of pellets.

*X-ray photoelectron spectroscopy (XPS)* measurements were performed at a base pressure of  $5 \times 10^{-10}$  mbar in a SPECS GmbH spectrometer equipped with a monochromatic Mg K $\alpha$  source ( $h\nu = 1253.6$  eV) and a PHOIBOS 100 hemispherical analyzer. All the samples were dispersed in H<sub>2</sub>O (1 wt.%), and after short sonication and stirring, a minute quantity of the suspensions was drop cast on silicon wafers and left to dry in air before transfer to ultrahigh vacuum. The energy resolution was set to 0.3 eV, and the photoelectron take-off angle was 45° with respect to the surface normal. The recorded spectra were the average of 3 scans with the energy step set to 0.05 eV and dwell time 1 s. All binding energies were referenced to the C 1 s core level at 284.8 eV. The spectral analysis included a Shirley background subtraction and peak deconvolution employing mixed

Gaussian–Lorentzian functions, in a least-squares curve-fitting program (WinSpec) developed at the Laboratoire Interdisciplinaire de Spectroscopie Electronique, University of Namur, Belgium.

The morphological characteristics of the catalyst samples were examined by *scanning electron microscopy (SEM)* on two systems, i.e., JEOL 6300 and JEOL JSM-6390LV, with magnification ability from 10 up to 300,000, both equipped with an *energy dispersive spectroscopy (EDS)* system for *X-ray microanalysis* (OXFORD ISIS 2000) operating at 20 kV. All the catalyst samples were placed on a double-sided carbon tape attached to an aluminum stub and were gold-sputtered to avoid charging effects. SEM images of the particles were obtained at different magnifications. For the point-EDS analyses, the corresponding spectra were recorded for 200 min in order to achieve a good signal-to-noise ratio. For the elemental mapping experiments, the particles were embedded in epoxy resin, ground, polished and then coated with gold, and spectra were recorded (30–120 min) on the flat cross-section surfaces of various particles.

*Transmission Electron Microscopy (TEM)* and *high-resolution TEM (HRTEM)* images were obtained on a high resolution JEOL-2100LaB6 instrument operating at 200 kV, equipped with a high resolution ORIUS SC1000 CCD camera. The samples were prepared by dipping holey-carbon-coated 200 mesh copper grids directly into powders.

The reduction characteristics of nickel oxide or other phases on pure supports (i.e., SiO<sub>2</sub>, Al<sub>2</sub>O<sub>3</sub> and USY zeolite) was studied by *temperature programmed reduction with H<sub>2</sub>* (*TPR-H<sub>2</sub>*). The TPR-H<sub>2</sub> experiments were performed in a gas flow system comprising a quartz tubular fixed-bed micro-reactor connected to a quadrupole mass spectrometer (Omnistar, Balzers, Balzers, Liechtenstein) for on-line analysis of the gases. Typically, the catalyst sample (0.2 g) was loaded in the quartz reactor and pretreated under 5% O<sub>2</sub>/He flow (50 cm<sup>3</sup>/min) for 30 min at 600 °C, followed by cooling at 30 °C. The temperature was then raised from 30 to 950 °C with a heating rate of 10 °C/min in a 5% H<sub>2</sub>/He flow (50 cm<sup>3</sup>/min). The main (*m/z*) fragments registered were: H<sub>2</sub>= 2, H<sub>2</sub>O = 18, CO = 28 and He = 4.

### 3. Results and Discussion

#### 3.1. Chemical Composition and Content of Nickel

The content of nickel and most abundant metals in the equilibrium FCC catalysts (Ecat) received from various refineries and the Ni-deposited FCC catalysts prepared following the Mitchell impregnation method [18] and the CPS deactivation protocol [21,22], are shown in Table 1. The Ni content of the Ni-loaded pure FCC catalysts components, i.e., Ni/Al<sub>2</sub>O<sub>3</sub>, Ni/SiO<sub>2</sub> and Ni/USY zeolite, are also shown in Table 1. The Ni content of the Ecat samples received from a collection point after the regenerator of the FCC unit of different refineries ranged between ca. 1300 and 5140 ppm Ni (corresponding to ~1650–6540 ppm NiO), in accordance with previous reports [5,8,23–25]. Ni content in Ecats depends mainly on the feedstock type (content of Ni compounds) and time on stream in the FCC continuous process. In an effort to better simulate and understand the state of Ni in the actual Ecats, the lab-prepared fresh FCC catalysts were loaded with 1000 to 10,000 ppm Ni, while the pure supports of SiO<sub>2</sub>, Al<sub>2</sub>O<sub>3</sub> and USY zeolite were loaded with a wider range of concentrations, i.e., from 150 to as high as 200,000 ppm Ni.

**Table 1.** Chemical composition of spent equilibrium FCC catalysts and lab-prepared Ni-loaded catalysts.

Sample	Ni (e) (ppm)	V (ppm)	Fe (wt.%)	Na (wt.%)	REO (wt.%)	Al <sub>2</sub> O <sub>3</sub> (wt.%)
<i>SiO<sub>2</sub>-Ni-X</i> <sup>(a)</sup>						
X = 1000, 2500, 5000, 10,000, 15,000, 20,000	934, 2129, 4485, 10,990, 17,030, 16,510	-	-	-	-	-

<b>SiO<sub>2</sub>-Ni-oc-X</b> <sup>(b)</sup>							
X = 500, 1000, 2500, 5000, 10,000, 15,000, 20,000	X = 887, 2190, 5561, 10,960, 17,100, 24,100	-	-	-	-	-	-
<b>SiO<sub>2</sub>-CH-Ni-oc-X</b> <sup>(c)</sup>							
X = 1000, 2500, 5000, 10,000, 15,000, 20,000	X = 893, 2437, 5626, 12,100 19,700, 24,830	-	-	-	-	-	-
<b>Al<sub>2</sub>O<sub>3</sub>-CH-Ni-oc-X</b> <sup>(c)</sup>							
X = 1000, 2500, 5000, 10,000, 15,000, 20,000, 100,000, 200,000	Nominal values	-	-	-	-	-	rest
<b>USY-CH-Ni-oc-X</b> <sup>(c)</sup>							
X = 1000, 2500, 5000, 10,000, 15,000, 20,000, 50,000	Nominal values	-	-	0.03	-	-	11.2
<b>BLF-CAT-X</b> <sup>(d)</sup>							
X = 1000, 2500, 5000, 10,000	Nominal values 10,000/9547	traces <sup>(f)</sup>	0.26	0.17	2.2	44	
<b>BLB-CAT-X</b> <sup>(d)</sup>							
X = 1000, 2500, 5000, 10,000	Nominal values 10,000/10,510	traces <sup>(f)</sup>	0.26	0.17	2.2	44	
<b>Ecat-2</b> <sup>(g)</sup> (B-CAT-2M)	4327	6153	0.73	0.26	2.1	40.2	
<b>Ecat-3</b> (B-CAT-3M)	3553	4761	0.62	0.40	4.6	53.6	
<b>Ecat-4</b> (B-CAT-4M)	2546	5009	0.89	0.26	2.7	41.0	
<b>Ecat-5</b> (B-CAT-5M)	5141	1949	0.89	0.46	3.0	44.3	
<b>Ecat-6</b> (B-CAT-6M)	1297	2608	0.89	0.28	1.9	39.6	

<sup>(a)</sup> Prepared by incipient wetness using aqueous solutions of Ni(NO<sub>3</sub>)<sub>2</sub>·6H<sub>2</sub>O. <sup>(b)</sup> Prepared by incipient wetness using nickel octanoate ([CH<sub>3</sub>(CH<sub>2</sub>)<sub>6</sub>COO]<sub>2</sub>Ni) solution in mineral spirits, diluted further in hexane, <sup>(c)</sup> as in <sup>(b)</sup> but nickel octanoate solution was diluted in cyclohexane while the support was first impregnated with cyclohexane until incipient wetness, followed by impregnation with the appropriate amount/volume of the nickel octanoate solution. <sup>(d)</sup> Prepared by the Mitchell impregnated method using nickel octanoate in spirits/solvent, followed by the CPS laboratory deactivation protocol described above. <sup>(e)</sup> XRF analysis. <sup>(f)</sup> Chemical analysis data refer to the fresh FCC catalyst used to prepare this series, being similar to that of the Ni-loaded samples. <sup>(g)</sup> The antimony (Sb) content of the Ecat samples was 584, 25, 534, 1037, and 231 ppm for samples 2 to 6, respectively.

### 3.2. Qualitative and Quantitative Determination of NiO by PXRD

The quantitative determination of the NiO phase in FCC equilibrium catalysts (Ecat) is of high importance as its content will classify the material either as hazardous (e.g., when NiO is  $\geq 0.1$  wt.% in EU) or non-hazardous throughout its complete lifecycle including removal, transfer and disposal as waste [5,26]. Chemical analysis for the determination of total nickel content is not useful in this case as a substantial portion of Ni in the Ecat is

not in the form of NiO (bunsenite) but as Ni<sup>2+</sup> in NiAl<sub>2</sub>O<sub>4</sub>, as Ni<sup>2+</sup> inside the alumina matrix or in other oxidation states in Ni<sub>x</sub>Al<sub>y</sub>O<sub>z</sub> spinel-like phases or in nickel-antimony (Ni-Sb) compounds, as already explained in the Introduction section. Furthermore, if other Ni-passivation agents are included in the FCC catalyst, such as in boron-based technology, then more of the Ni can be kept at a less reduced state [27]. With regards to the capabilities of the powder X-ray diffraction (pxrd) method, these are limited by the amount and the relative size of the crystallites of the supported/embedded metal/metal oxide, in this case metallic Ni(0) or NiO. For small nanoparticle sizes (<10 nm) it may be difficult to observe the corresponding Bragg reflections, as these become broad with reduced intensities, while for larger particles, more sharp and intense reflections are observed. The conditions of Ni/SiO<sub>2</sub>, Al<sub>2</sub>O<sub>3</sub> and USY prototype catalysts preparation in the present study, related mainly to their final calcination at high temperatures (700–805 °C), as well as the treatment conditions of the FCC catalysts (Ecats from a collection point after the FCC regenerator and laboratory prepared and deactivated FCC samples, all of them being finally calcined at 594 °C prior to characterization), indicate that Ni should be present in the form of crystalline NiO phases. If nickel has been passivated with the help of Al-, Sb- or B-based compounds, corresponding crystalline phases that keep Ni at a higher oxidation state longer and inhibit its reduction, such as NiAl<sub>2</sub>O<sub>4</sub>, may also form, as mentioned above. Thus, the aim of this study was to determine the lower limits of Ni content at which NiO, NiAl<sub>2</sub>O<sub>4</sub> or related crystalline phases could be identified and, if possible, quantified on the basis of calibration curves between the integrated area of the most intense Bragg peak from high quality pxrd patterns and Ni content.

### 3.2.1. Ni/SiO<sub>2</sub> Samples

Representative PXRD patterns of SiO<sub>2</sub>-CH-Ni-oc samples, prepared via impregnation with Ni octanoate solution and diluted in cyclohexane using SiO<sub>2</sub> supports that had been previously impregnated to incipient wetness with cyclohexane (see experimental section), are shown in Figure 1. The inset in Figure 1, focuses on the 2θ range around the (2 0 0) reflection of NiO (bunsenite), which is the strongest one. The acquisition time for the experiments in the range 41–45° 2θ was 13 s/step (step size 0.02° 2θ) in order to improve the signal-to-noise ratio and the accuracy of the measurements compared with the time of 3 s/step used to record full range patterns (10–90° 2θ). As it can be seen from the slow scan patterns, weak peaks can be identified even for the sample containing 2500 ppm Ni (which corresponds to 3182 ppm NiO or ~0.318 wt.% NiO) but not for the sample with 1000 ppm Ni. When these two samples were measured with an even longer acquisition time, i.e., 30 s/step, a slight improvement in the signal-to-noise ratio of the pattern was observed for the 2500 ppm Ni sample, whereas no peak could still be identified for the sample containing 1000 ppm Ni (Figure 2a). The effect of intense calcination, such as that at 805 °C for 12 h, was also examined (Figure 2b). The (2 0 0) reflection for the samples containing 2500, 5000 and 10,000 ppm Ni became slightly narrower after intense calcination and this was reflected in the crystal size of NiO determined by the Scherrer equation. For example, the crystal size of the 5000 and 10,000 ppm Ni samples increased from 10.3 and 11.8 nm to 11.8 and 12.7 nm, respectively. Although, close to experimental error, ca. 3%, these results are indicative of slight changes in the NiO crystals, which can be more pronounced in the case of severely steamed equilibrium FCC catalysts. However, the integrated peak area did not change significantly, and this may allow for the construction of a calibration curve based on laboratory prepared Ni/SiO<sub>2</sub> samples that could be applied for semi-quantitative determination of the NiO (bunsenite) phase in Ecats. Such curves are constructed and discussed below.

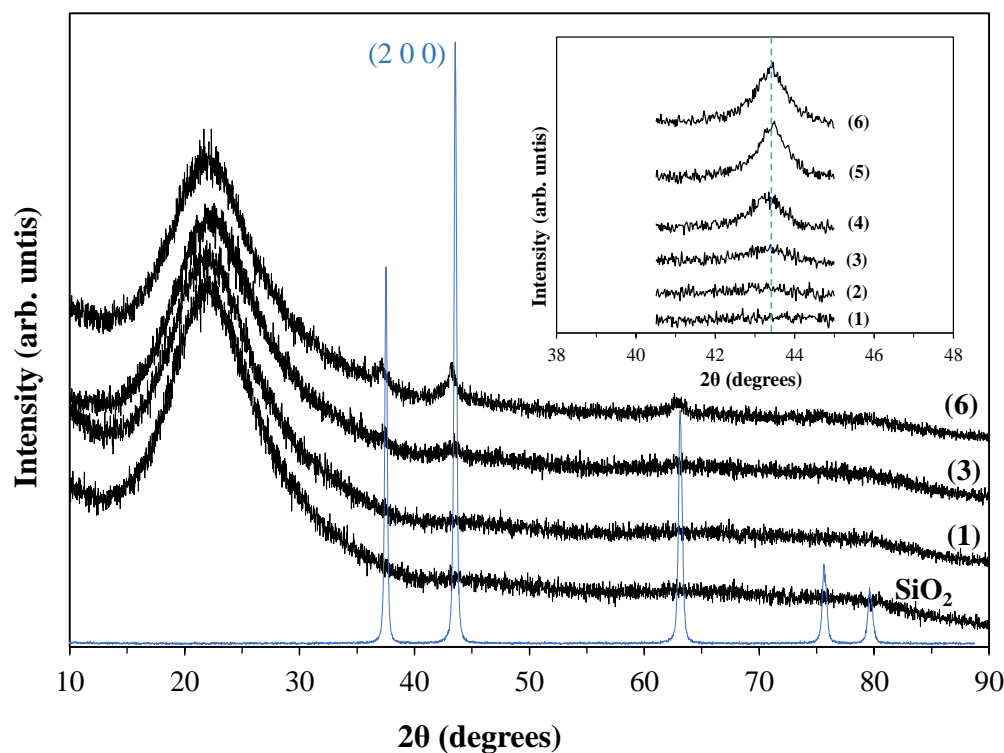


**Figure 1.** PXRD patterns of  $\text{SiO}_2\text{-CH-Ni-oc-X}$  samples, prepared via impregnation of  $\text{SiO}_2$  with Ni octanoate solution diluted in cyclohexane (see experimental section); X: (1) 1000 ppm Ni, (2) 2500 ppm Ni, (3) 5000 ppm Ni, (4) 10,000 ppm Ni, (5) 15,000 ppm Ni, and (6) 20,000 ppm Ni. The dashed line in the inset graph represents the (2 0 0) reflection of  $\text{NiO}$  (bunsenite). The pattern of pure  $\text{NiO}$  (bunsenite structure) is also shown for comparison (blue pattern).

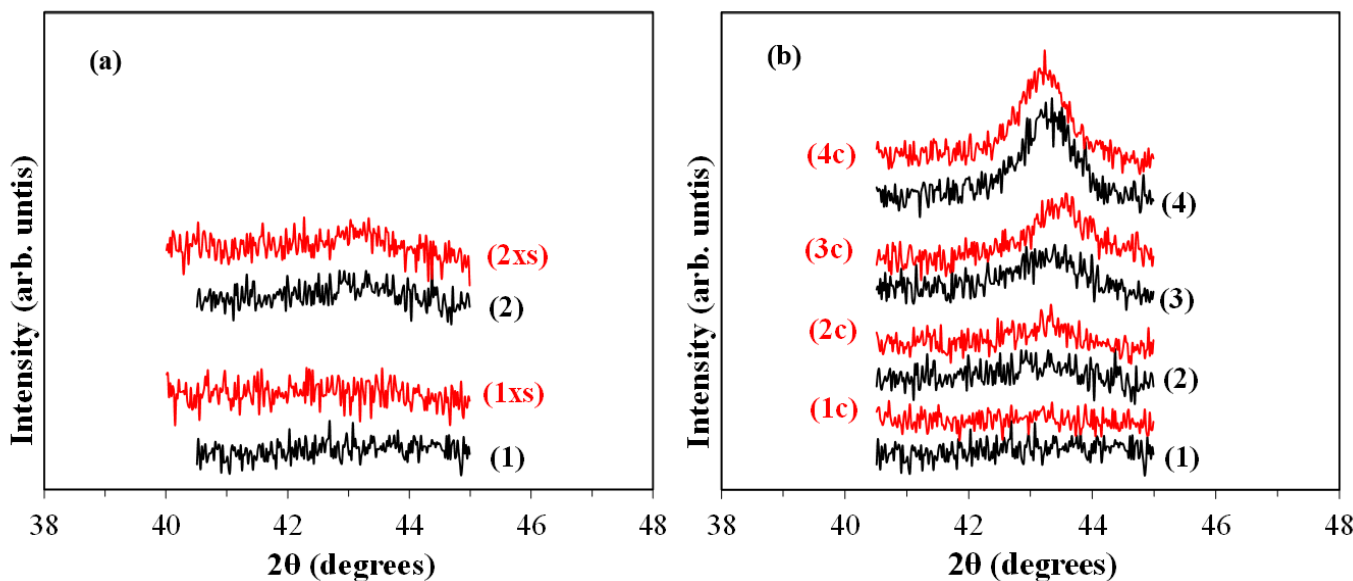


**Figure 2.** (a) Effect of pxrd scan conditions on the quality of the obtained patterns: Patterns (1xs) and (2xs) refer to the samples  $\text{SiO}_2\text{-CH-Ni-oc-X}$  with 1000 and 2500 ppm Ni, respectively, for which an acquisition time of 30 s/step was applied, compared with the corresponding patterns (1) and (2), which were obtained with an acquisition time of 13 sec/step. (b) Effect of intense calcination on the shape and intensity of the Bragg reflections: Patterns (1,2,3,4) refer to the parent samples (i.e., calcined at  $700\text{ }^\circ\text{C}$ , 3 h), and patterns (1c, 2c, 3c, 4c) refer to the corresponding samples after additional calcination at  $805\text{ }^\circ\text{C}$ , 12 h (acquisition time of 13 s/step).

The corresponding short range ( $41\text{--}45^\circ 2\theta$ ) pxrd patterns for the other two series of Ni/SiO<sub>2</sub> samples, i.e., using aqueous solutions of nickel nitrate or nickel octanoate solutions diluted in hexane, are presented in Figure 3. As in the case of the SiO<sub>2</sub>-CH-Ni-oc samples, it was difficult to identify the (2 0 0) reflection of NiO in the patterns of the samples with 1000 ppm Ni. This reflection becomes visible for the 2500 ppm Ni sample and its intensity increases with increasing Ni content.

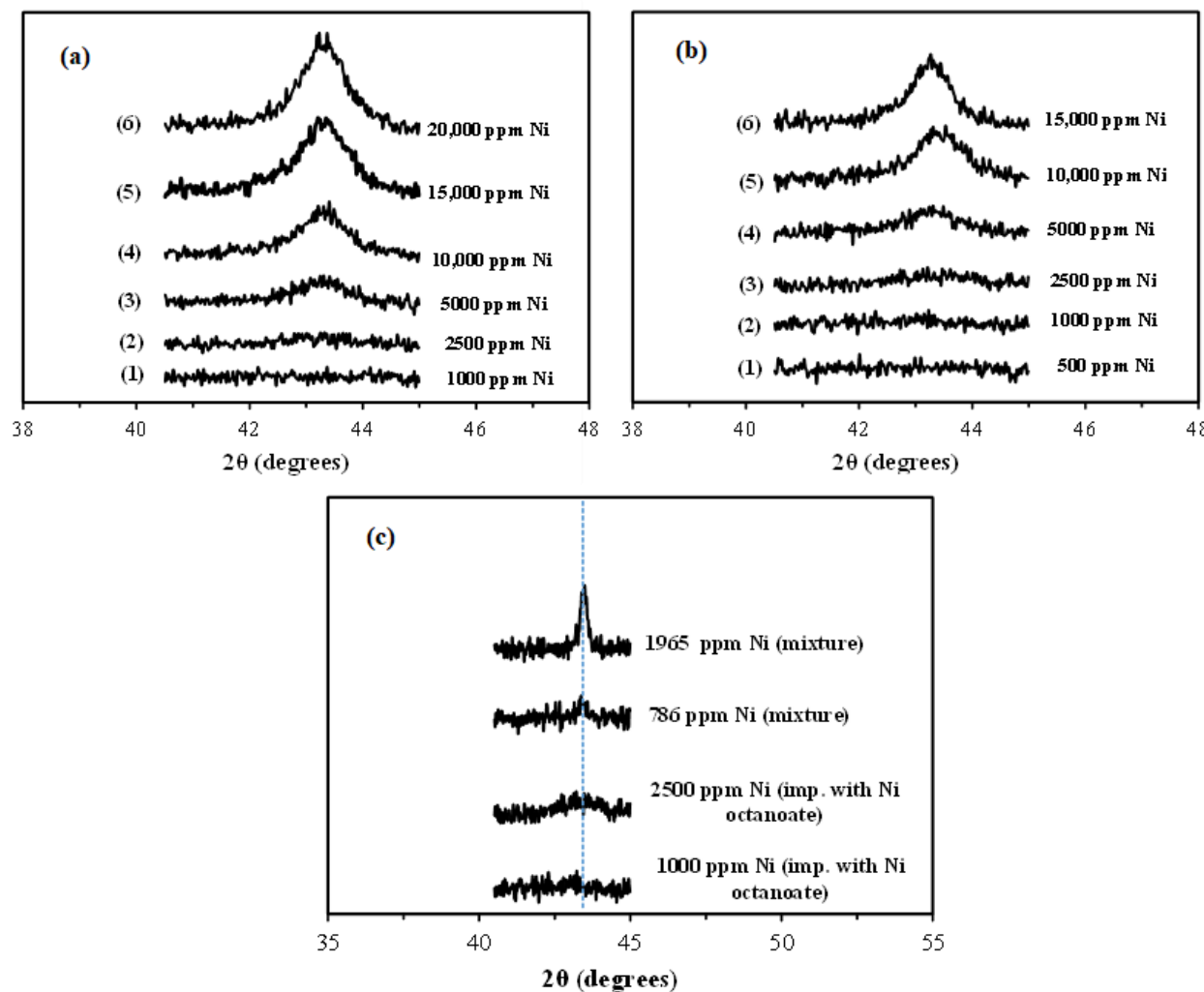


**Figure 3.** XRD patterns. (a) SiO<sub>2</sub>-Ni-X samples prepared via impregnation of SiO<sub>2</sub> with aqueous solutions of nickel nitrate; X: (1) 1000 ppm Ni, (2) 2500 ppm Ni, (3) 5000 ppm Ni, (4) 10,000 ppm Ni, (5) 15,000 ppm Ni, and (6) 20,000 ppm Ni. (b) SiO<sub>2</sub>-Ni-oc-X samples prepared via impregnation with Ni octanoate solution diluted in hexane (see experimental section); X: (1) 500 ppm Ni, (2) 1000 ppm Ni, (3) 2500 ppm Ni, (4) 5000 ppm Ni, (5) 10,000 ppm Ni, and (6) 15,000 ppm Ni. (c) SiO<sub>2</sub>-Ni-oc-X samples with 1000 and 2500 ppm Ni, and two physical mixtures of bulk NiO with SiO<sub>2</sub> at two levels of Ni content, i.e., 786 and 1965 ppm Ni (corresponding to 1000 and 2500 ppm NiO). The dashed line in the graphs represents the (2 0 0) reflection of NiO (bunsenite).

In order to further investigate the detectability limits of the PXRD measurements for the NiO-based materials, the patterns of two physical mixtures of bulk crystalline NiO (prepared by calcination of Ni(NO<sub>3</sub>)<sub>2</sub> salt at 700 °C for 3 h) with calcined SiO<sub>2</sub> were also recorded and are presented in Figure 3c. The Ni/NiO contents of the two physical mixtures were Ni 786 ppm/NiO 1000 ppm for the first, and Ni 1965 ppm/NiO 2500 ppm for the second sample. The (2 0 0) reflection of bulk NiO can now be observed even for the mixture containing 786 ppm Ni (or 1000 ppm NiO). Furthermore, the NiO peak for the 1965 ppm Ni/2500 ppm NiO mixture exhibits a sharp shape compared with the very broad

peaks observed for the various impregnated Ni/SiO<sub>2</sub> samples with Ni contents as high as 20,000 ppm (Figure 3a,b). These results clearly demonstrate that pxd<sup>r</sup>d can detect bulk NiO at even the low end of the studied concentration regime (ca. 1000 ppm NiO or 786 ppm Ni) in solid mixtures, but higher Ni loadings (ca. ≥2500 ppm) are required when Ni is highly dispersed over porous supports such as SiO<sub>2</sub>, Al<sub>2</sub>O<sub>3</sub> and zeolites, including FCC catalysts.

The integrated peak area of the (2 0 0) reflection of NiO (bunsenite) at ~43.3° 2θ was used to plot calibration curves by utilizing the above presented Ni/SiO<sub>2</sub> samples as external standards. The range of Ni loading was kept at relatively low values, ca. below 20,000 ppm, in order to be more representative of the Ni content in typical equilibrium catalysts from actual FCC units. As can be seen in Figure 4, linear correlations with coefficient  $r^2 > 0.992$  were obtained for all three series of Ni/SiO<sub>2</sub> samples, prepared by different procedures. For example, for the SiO<sub>2</sub>-CH-Ni-oc series of samples, the derived equation was  $I_{(200)} = 1.2453[\text{Ni}]$  with coefficient  $r^2 = 0.9987$ ; this equation was used for the quantification of NiO (bunsenite) in the commercial FCC catalysts.

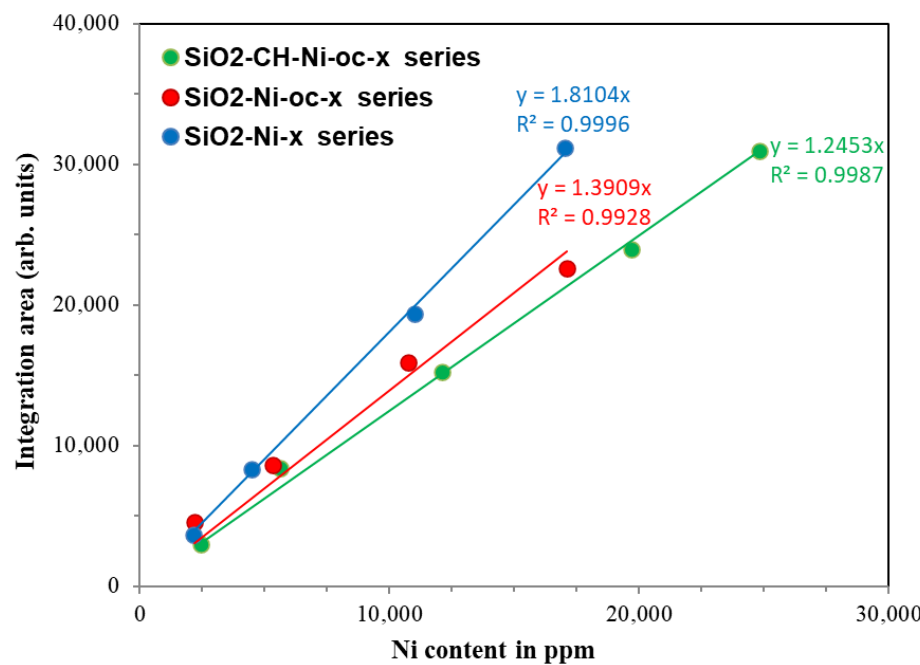


**Figure 4.** Correlation of the integrated intensity of the (2 0 0) reflection of NiO (bunsenite) versus Ni content of the three series of Ni-loaded SiO<sub>2</sub> samples (linear fit was calculated with zero intercept).

As discussed above, the more intense calcination of the Ni/SiO<sub>2</sub> samples at 805 °C for 12 h, being initially calcined at 700 °C for 3 h, had a minor effect on the integrated area of the (2 0 0) reflection. This can be clearly seen from the plots of Figure 5, where the calibration lines of the two sets of samples (mildly and more severely calcined) fall on top of each other.

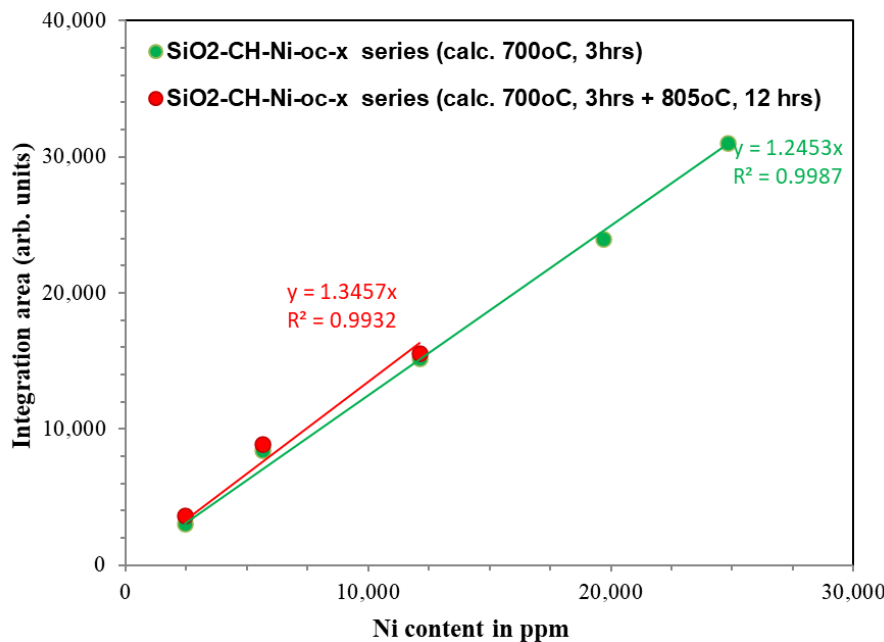


**Figure 5.** Effect of calcination severity on the correlation of the integrated intensity of the (2 0 0) reflection of NiO (bunsenite) versus Ni content for the same series of Ni-loaded SiO<sub>2</sub> samples (linear fit was calculated with zero intercept).

### 3.2.2. Ni/Al<sub>2</sub>O<sub>3</sub> and Ni/USY Samples

The formation of NiO phases has been also investigated on alumina, using a typical  $\gamma$ -Al<sub>2</sub>O<sub>3</sub> support that was impregnated with Ni following procedure (c) described in the experimental section, i.e., using Ni octanoate solution diluted in cyclohexane and the Al<sub>2</sub>O<sub>3</sub> support being previously impregnated to incipient wetness with cyclohexane. This procedure better simulates the conditions of Ni deposition on the FCC catalyst during the cracking reactions (in the FCC riser) in terms of pore coverage/blockage with hydrocarbon vapours. The pxrd patterns of the derived samples are shown in Figure 6, and are compared with the patterns of bulk NiO and NiAl<sub>2</sub>O<sub>4</sub>. The pattern of the parent Al<sub>2</sub>O<sub>3</sub> calcined at 700 °C is typical of cubic  $\gamma$ -Al<sub>2</sub>O<sub>3</sub>[28,29](JCPDS 75-0921). Identification of reflections attributed to NiO (bunsenite) phase was not possible in the Ni/Al<sub>2</sub>O<sub>3</sub> samples with up to 100,000 ppm Ni (i.e., 10 wt.% Ni or 12.7 wt.% NiO). It is thus shown that well-formed NiO crystals are not formed on Al<sub>2</sub>O<sub>3</sub> even at ca. 10 wt.% Ni loading, indicating the Ni-trapping effect of alumina, as discussed in the Introduction. On the other hand, the most prominent reflections of NiO, i.e., (2 0 0) at ~43.3° and (2 2 0) at ~62.9° 2θ, exhibited high intensities in the pattern of the sample with 20 wt.% Ni (25.4 wt.% NiO), whereas the reflection (1 1 1) at ~37.2° 2θ was superimposed by the (3 1 1) reflection of Al<sub>2</sub>O<sub>3</sub>. The NiO reflections of relatively lower intensity in the range 75–80° 2θ were also clearly observable in the 20 wt.% Ni/Al<sub>2</sub>O<sub>3</sub> sample. A closer look at the patterns of the Ni loaded samples with 5000 to 100,000 ppm Ni compared with that of pure Al<sub>2</sub>O<sub>3</sub> revealed the progressive slight shift of the (4 0 0) and (4 4 0) reflections of Al<sub>2</sub>O<sub>3</sub> at ~46.2° and 67.1° 2θ, respectively, to lower angles towards the corresponding characteristic reflections (4 0 0) and (4 4 0) of bulk NiAl<sub>2</sub>O<sub>4</sub> [30] (Figure 6a,b). This is indicative of an expansion of the unit cell of Al<sub>2</sub>O<sub>3</sub> due to the insertion of Ni<sup>2+</sup> cations inside the lattice and the formation of Ni<sub>x</sub>Al<sub>2</sub>O<sub>3+x</sub> spinel-like phases [5,31]. The more intense calcination of the 20 wt.% Ni/Al<sub>2</sub>O<sub>3</sub> sample at 805 °C for 12 h had no significant effect on the features of the pxrd pattern, although the slight increase of intensity of the (1 1 1) and (5 1 1) reflections could be related to enhanced formation of crystalline NiAl<sub>2</sub>O<sub>4</sub> spinel phase (pattern 8c in Figure 6a,b).

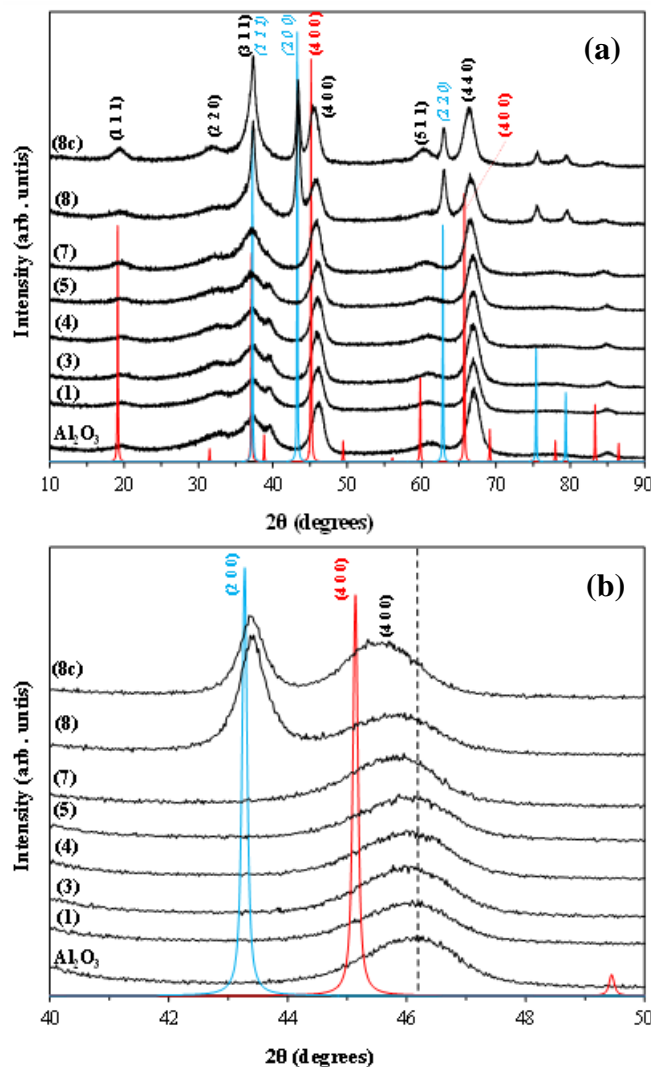


**Figure 6.** (a) PXRD patterns of Al<sub>2</sub>O<sub>3</sub>-CH-Ni-oc-X samples, prepared via impregnation of  $\gamma$ -Al<sub>2</sub>O<sub>3</sub> with Ni octanoate solution diluted in cyclohexane (see experimental section); X: (1) 1000 ppm Ni, (3) 5000 ppm Ni, (4) 10,000 ppm Ni, (5) 15,000 ppm Ni, (7) 100,000 ppm Ni, (8) 200,000 ppm Ni, and (8c) sample with 200,000 ppm Ni calcined at 805 °C, 12 h, in addition to the typical calcination at 700 °C, 3 h. (b) Enlarged view in the range 40–50° 2θ (the dashed line indicates the center of the reflection attributed to  $\gamma$ -Al<sub>2</sub>O<sub>3</sub>). The patterns of NiO (blue pattern) and NiAl<sub>2</sub>O<sub>4</sub> (red pattern) are also shown for comparison.

Representative PXRD patterns of Ni/USY zeolite samples which were prepared following the procedure (c) described in the experimental section, i.e., using Ni octanoate solution diluted in cyclohexane and the USY support being previously impregnated to incipient wetness with cyclohexane, are shown in Figure S1 (Supplementary Material). The PXRD pattern of USY is typical of this type of zeolite [32,33], but no reflections characteristics of bulk NiO or NiAl<sub>2</sub>O<sub>4</sub> could be detected even at the relatively high loading of 50,000 ppm Ni (5 wt.% Ni or 6.4 wt.% NiO). This is in accordance with the results shown for Al<sub>2</sub>O<sub>3</sub> above, as USY zeolites contain substantial amounts of Al<sub>2</sub>O<sub>3</sub>, ca. 6–7 wt.%, thus being capable to passivate Ni.

### 3.2.3. Ni-Loaded FCC and Ecat Samples

The PXRD patterns of the Ni-loaded actual FCC catalyst samples are shown in Figure 7 (for the BLF-CAT-x series, conventional Ni-passivation, not containing boron-based passivation) and Figure 8 (for the BLB-CAT-x series, with boron-based passivation). The dominant reflections are attributed to zeolite Y (USY), being the typical main zeolitic

component of an FCC catalyst [5,6,32,34,35], while reflections in the range of 45–70°  $2\theta$ , i.e., the (4 0 0) and (4 4 0) reflections at ~46° and 67°  $2\theta$ , respectively, originate from  $\text{Al}_2\text{O}_3$  used as the matrix. The (2 0 0) reflection of  $\text{NiO}$  (bunsenite) at ~43.3°  $2\theta$  is clearly visible only in the BLF-CAT-4 sample (with 10,000 ppm Ni), while very weak signals could also be detected for the samples with 2500 and 5000 ppm Ni (Figure 7). The other two strong reflections of  $\text{NiO}$ , i.e., at ~37.2°  $2\theta$  (1 1 1) and at ~62.9°  $2\theta$  (2 2 0), cannot be identified even in the 10,000 ppm Ni sample. Similar patterns and  $\text{NiO}$  peak intensities are observed for the BLB-CAT-x samples (Figure 8), with the (2 0 0)  $\text{NiO}$  reflection of the BLB-CAT-4 (10,000 ppm Ni) being of slightly lower intensity (integrated peak area) compared with that of the corresponding BLF-CAT-4 sample. No  $\text{NiAl}_2\text{O}_4$  reflections could be observed in any samples, nor could any clear shift of the characteristic reflections of  $\text{Al}_2\text{O}_3$ , (4 0 0) and (4 4 0), towards lower angles be identified, as was shown above for the  $\text{Ni}/\text{Al}_2\text{O}_3$  samples containing  $\geq 5000$  ppm Ni.

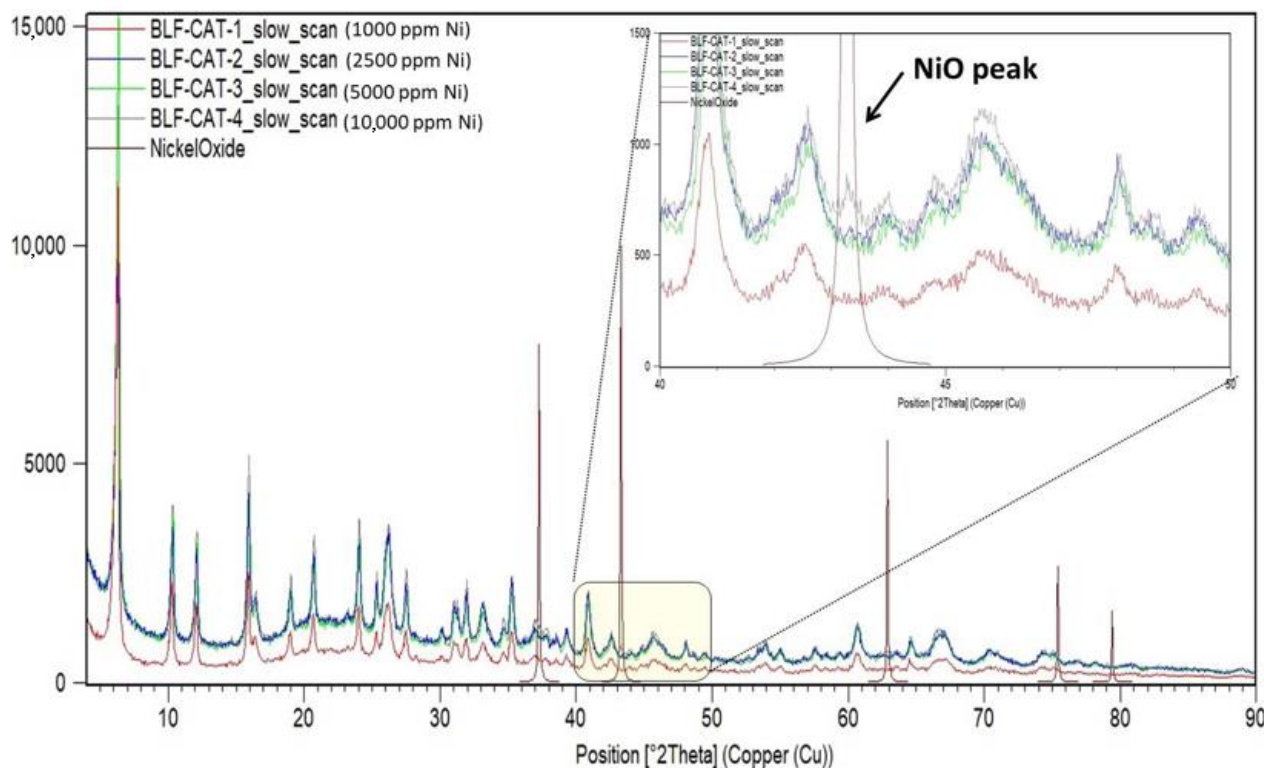


**Figure 7.** PXRD patterns of BLF-CAT-x samples which are industrial FCC catalysts loaded with increasing amounts of Ni and deactivated in the lab following typical cyclic propylene steaming (CPS) deactivation protocols. The pattern of  $\text{NiO}$  is also included for comparison, while the inset figure focuses on the  $2\theta$  region of 40 to 50°, which includes the most prominent reflection of  $\text{NiO}$ , i.e., (2 0 0) at ~43.3°.

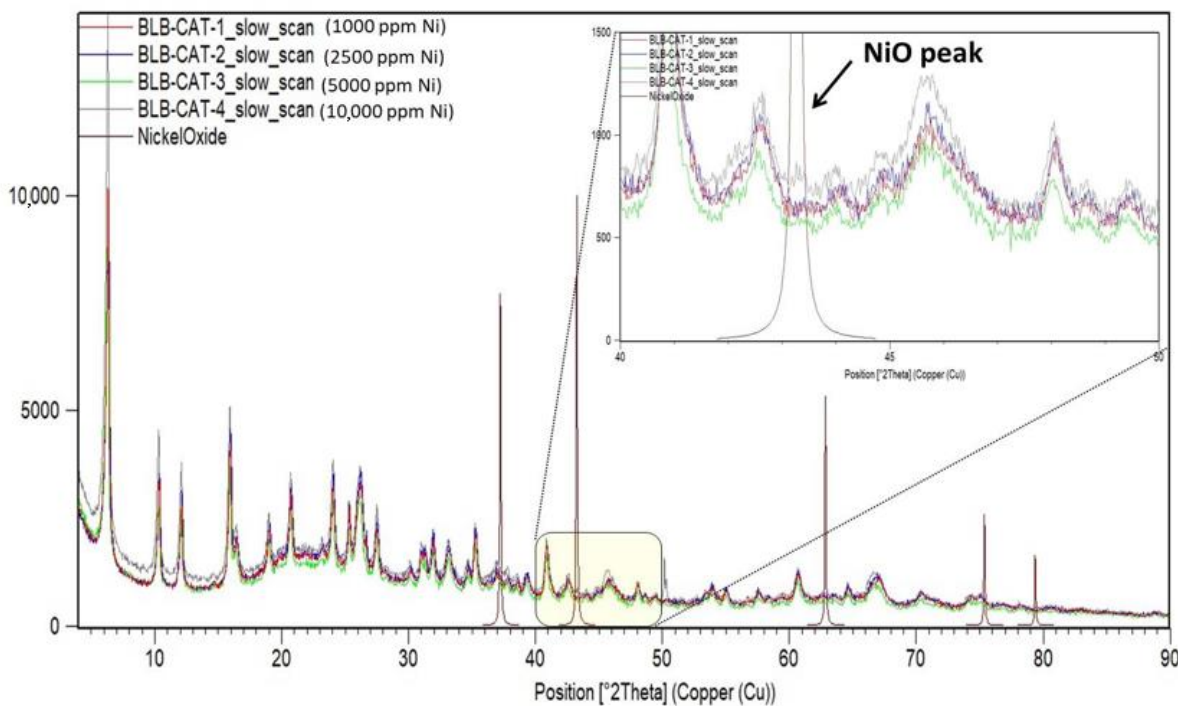


**Figure 8.** PXRD patterns of BLB-CAT-x samples which are industrial boron-containing FCC catalysts loaded with increasing amounts of Ni and deactivated in the lab following typical cyclic propylene steaming (CPS) deactivation protocols. The pattern of NiO is also included for comparison, while the inset figure focuses on the  $2\theta$  region of 40 to 50°, which includes the most prominent reflection of NiO, i.e., (2 0 0) at ~43.3°.

When compared with the detection limits of the (2 0 0) NiO reflection in  $\text{SiO}_2$  ( $\geq 2500$  ppm Ni for impregnated samples and  $\geq 800$  ppm Ni for physical mixtures of bulk NiO and  $\text{SiO}_2$ ),  $\text{Al}_2\text{O}_3$  ( $\geq 100,000$  ppm Ni) and USY zeolite ( $\geq 50,000$  ppm Ni), it is obvious that the limits for laboratory Ni-loaded/CPS deactivated FCC catalysts are closer to those of impregnated Ni/ $\text{SiO}_2$  samples, as can be further verified by comparing the patterns in Figures 7 and 8 with those in Figure 1. It can thus be suggested that the presence of  $\text{Al}_2\text{O}_3$  phases in the FCC particle act as Ni passivators, while their efficiency depends on various parameters, such as the architecture of the FCC particle (i.e., a higher relative amount of  $\text{Al}_2\text{O}_3$  phases in the periphery of the FCC particle captures Ni in the form of  $\text{Ni}_x\text{Al}_2\text{O}_{3+x}$  phases, not allowing time for it to diffuse within the particle and crystallize/aggregate towards bulk NiO nanoparticles) or the severity of the treatment/deactivation of the catalyst (i.e., initially formed amorphous  $\text{Ni}_x\text{Al}_2\text{O}_{3+x}$  phases or very small NiO nanoparticles can evolve to larger NiO or  $\text{NiAl}_2\text{O}_4$  crystalline nanoparticles that can be detected by pxrd). Regarding the effect of boron, although a substantial lower content of NiO (bunsenite) phase was determined in the BLB-CAT-4 (10,000 ppm Ni) compared with the corresponding B-free BLF-CAT-4 sample (as discussed below on the basis of the constructed calibration line), more dedicated studies with higher amounts of boron and/or Ni are required in order to further study the passivating action of boron species by PXRD measurements.

The PXRD patterns of the Ecat (equilibrium FCC catalysts) samples with a total Ni content in the range of 1300 to 5140 ppm Ni obtained from different European refineries are shown in Figure 9. The patterns are similar to those of the BLF-CAT-x and BLB-CAT-x series. They do not contain any additional reflections attributed ZSM-5 zeolite-based additives which are usually added to the FCC (i.e., into the circulating catalyst inventory) to enhance the production of LPG (mainly propylene and butylenes) and increase the octane rating but with the penalty of decreasing the yield of gasoline [6,35–37]. The strongest reflection of the NiO (bunsenite) structure, i.e., the (2 0 0) reflection at ~43.3°  $2\theta$ , was

detectable in the patterns of the Ecats B-CAT-XM, with  $X = 2, 4, 5$  and  $6$ , which contained 4327, 2546, 5141 and 1297 ppm Ni, respectively.

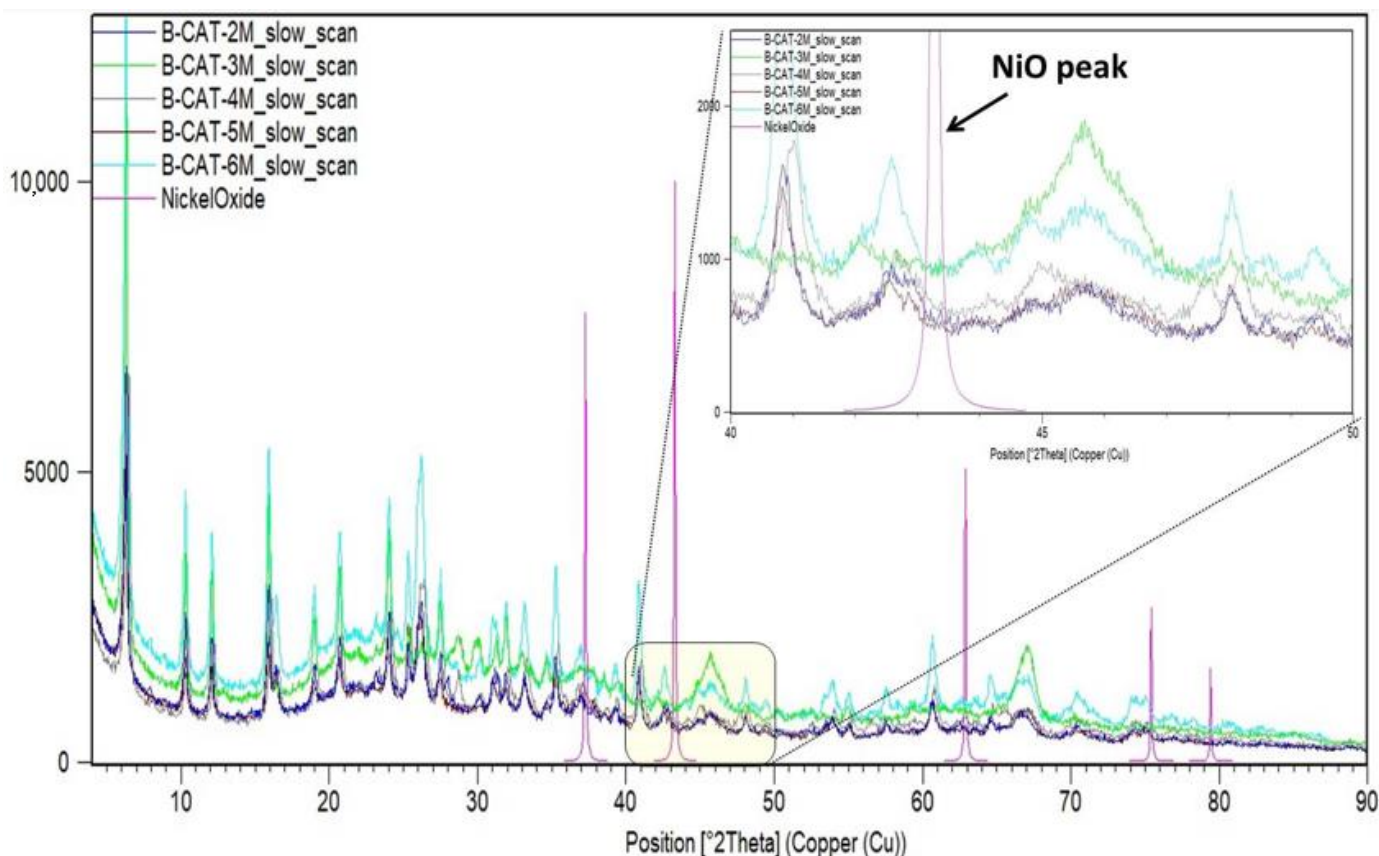


**Figure 9.** PXRD patterns of the Ecats (equilibrium FCC catalysts) samples with a total Ni content in the range of 1300 to 5140 ppm Ni. The pattern of NiO is also included for comparison. The inset figure focuses on the  $2\theta$  region of 40 to 50° which includes the most prominent reflection of NiO, i.e., (2 0 0) at  $\sim 43.3^\circ$ .

The integrated peak area of the (2 0 0) reflection was used to determine the portion of Ni that exists as NiO (bunsenite) phase in the samples of both series of Ni-loaded FCC catalysts by the use of the calibration line shown in Figure 4 that was constructed for the  $\text{SiO}_2\text{-CH-Ni-oc-X}$  samples. The obtained data as ppm Ni and NiO are shown in Table 2. It is clear that the calculated NiO content is significantly low i.e., less than 10% of the total Ni content in the Ni-loaded FCC catalysts, especially in the samples containing up to 5000 ppm Ni. In the case of the 10,000 ppm Ni samples, the NiO portion is slightly higher, reaching 14% in the BLF-CAT-4 sample and 7% in the BLB-CAT-4 sample. This is also a strong indication that the presence of boron in the latter sample has a measurable (based on PXRD) effect on passivating Ni, not allowing the formation of bulk nano-crystalline NiO, that could then be easily reduced in the FCC riser to the undesirable Ni(0) metallic state. The content of NiO was also calculated for the equilibrium FCC catalysts (Ecats) collected from different refineries. The obtained data (Table 2) shows that the portion of NiO is higher in these commercial Ecats, i.e., ranging from 3 to 27% of total Ni, compared with the Ni-loaded and laboratory deactivated FCC catalysts. As discussed above, the extent to which Ni is transformed to NiO does not depend only on its total content in the catalyst, but also on the architecture and technological features of the FCC catalyst and its history (i.e., conditions it was subjected to as consequence of the type of operation and feed process as well as operational parameters of the unit).

**Table 2.** Portion of Ni existing as NiO in the Ni-loaded FCC catalysts.

Sample	Total Ni Content (ppm)	Ni * (ppm)	Ni as NiO (ppm)
BLF-CAT-1	1000	-	-
BLF-CAT-2	2500	217	276
BLF-CAT-3	5000	243	310
<b>BLF-CAT-4</b>	<b>10,000</b>	<b>1391</b>	<b>1770</b>
BLB-CAT-1	1000	-	-
BLB-CAT-2	2500	-	-
BLB-CAT-3	5000	230	293
<b>BLB-CAT-4</b>	<b>10,000</b>	<b>722</b>	<b>919</b>
B-CAT-2M	4327	359	456
B-CAT-3M	3553	-	-
B-CAT-4M	2546	108	137
B-CAT-5M	5141	150	191
B-CAT-6M	1297	348	442

\* The relative standard error was estimated to 5%.

### 3.3. Fourier-Transform Infrared Spectroscopy (FTIR)

The FTIR spectra of representative Ni-impregnated samples, i.e., Ni/Al<sub>2</sub>O<sub>3</sub>, Ni/SiO<sub>2</sub> and Ni/USY, are shown in Figure 10; the corresponding spectra of the full mid-IR region are shown in Figure S2 (Supplementary Material). The spectra of the bulk NiO and NiAl<sub>2</sub>O<sub>4</sub>/NiO mixed-phase samples are also included for comparison. The spectra of parent γ-Al<sub>2</sub>O<sub>3</sub>, amorphous SiO<sub>2</sub> and USY zeolite are typical for these types of materials [33,38,39] (in the case of USY, the amount of zeolite in the KBr pellet was relatively high in order to focus/enlarge the region of 400–900 cm<sup>-1</sup>, leading to poor resolution of the main peak at ~1050 cm<sup>-1</sup>). The spectrum of bulk NiO exhibits a broad band at ~455 cm<sup>-1</sup>, and that of mixed NiAl<sub>2</sub>O<sub>4</sub>/NiO also contains this band, as well as another two broad bands, i.e., at ~495 and 735 cm<sup>-1</sup>, which are attributed to NiAl<sub>2</sub>O<sub>4</sub> [40,41]. The spectrum of Al<sub>2</sub>O<sub>3</sub>-CH-Ni-oc-7 with 10 wt.% Ni exhibits a clear band at ~735 cm<sup>-1</sup> and, to a lesser extent, one at ~495 cm<sup>-1</sup>. The NiO band at ~455 cm<sup>-1</sup> is superimposed by typical SiO<sub>2</sub> and USY bands in the spectra of samples SiO<sub>2</sub>-CH-Ni-oc-5 and USY-CH-Ni-oc-6, respectively, whereas the bands attributed to NiAl<sub>2</sub>O<sub>4</sub> cannot be identified in the spectrum of the Ni/USY sample. Accordingly, bands attributed to NiO or NiAl<sub>2</sub>O<sub>4</sub> phases could not be observed in the Ni-loaded FCC catalysts or the Ecats, due to the relatively low content of Ni and the masking effect of zeolite or silica bands.

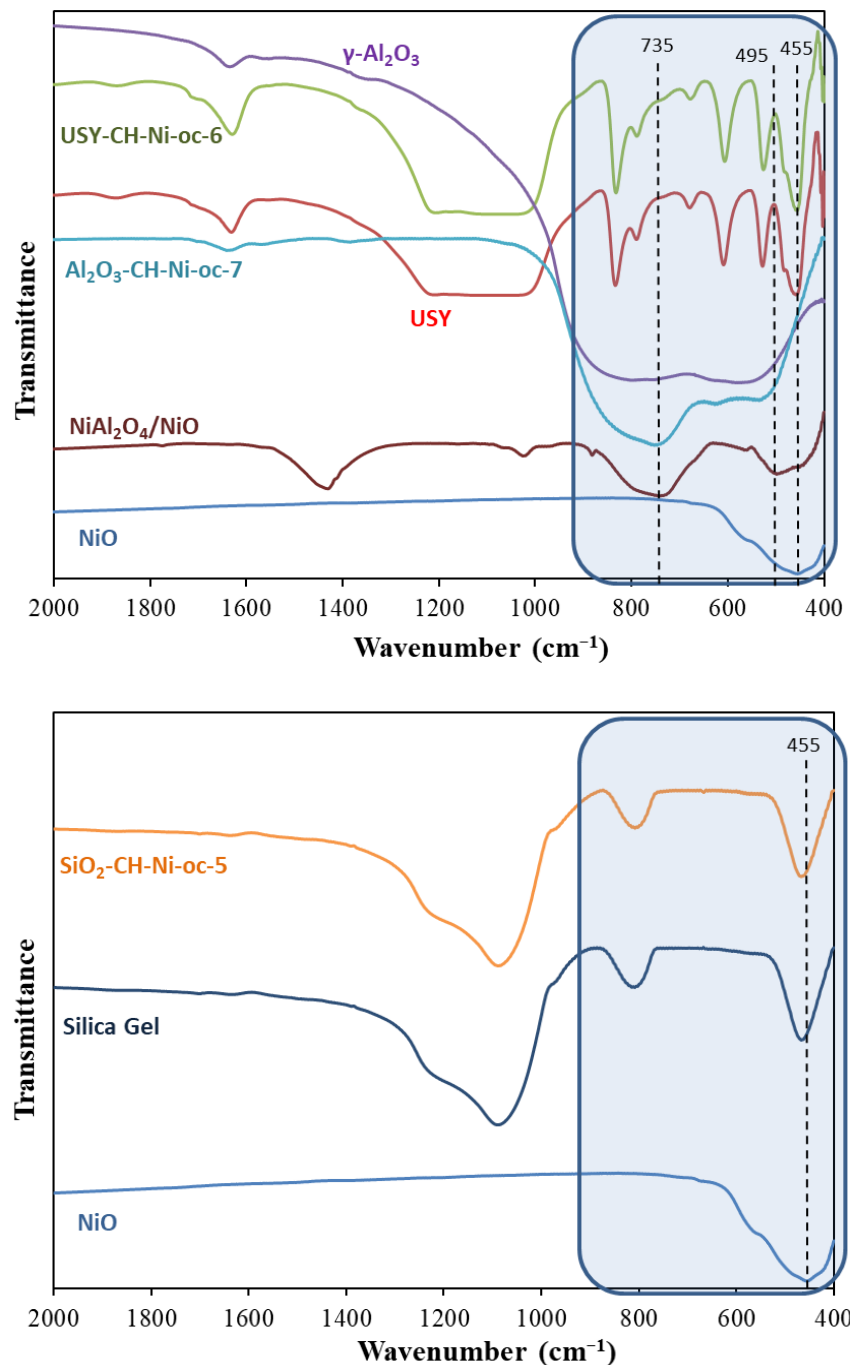
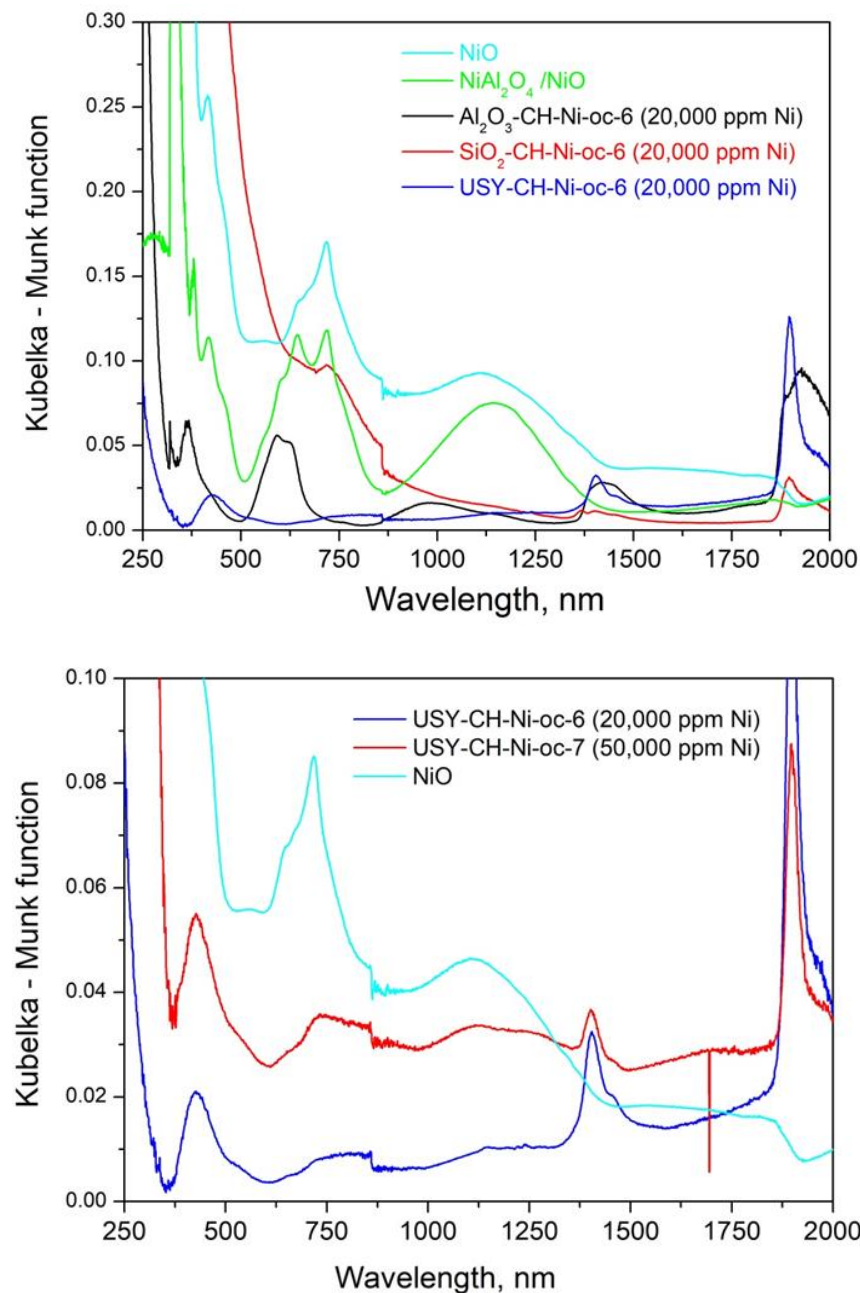


**Figure 10.** FTIR spectra of representative Ni-impregnated materials:  $\text{SiO}_2\text{-CH-Ni-oc-5}$  (1.5 wt.% Ni),  $\text{Al}_2\text{O}_3\text{-CH-Ni-oc-7}$  (10 wt.% Ni), and USY-CH-Ni-oc-6 (2 wt.% Ni). The spectra of bulk  $\text{NiO}$ ,  $\text{NiAl}_2\text{O}_4/\text{NiO}$ , silica gel,  $\gamma\text{-Al}_2\text{O}_3$  and USY zeolite, are also included for comparison.

### 3.4. Diffuse Reflectance UV-Vis/Near IR

The diffuse reflectance UV-Vis-near IR spectra of representative samples are shown in Figure 11. Pure  $\text{NiO}$  shows a characteristic strong absorption in the visible region at 718 nm attributed to the  ${}^3\text{A}_{2g} \rightarrow {}^3\text{T}_{1g}$  d-d transition, with a shoulder near 646 nm associated with the weaker  ${}^3\text{A}_{2g} \rightarrow {}^1\text{E}_g$  transition [28,31,42]. The absorption band at 718 nm is also present in the representative Ni/SiO<sub>2</sub> sample, namely SiO<sub>2</sub>-CH-Ni-oc-6 (20,000 ppm Ni), in agreement with pxrd data, where  $\text{NiO}$  phase was detected. In contrast, in the respective Al<sub>2</sub>O<sub>3</sub> based sample with the same Ni loading, namely Al<sub>2</sub>O<sub>3</sub>-CH-Ni-oc-6 (20,000 ppm Ni), the spectrum in the visible region shows a doublet at 590 nm and 625 nm which is attributed to the presence of “isolated”  $\text{Ni}^{2+}$  cations, in full agreement with the pxrd results

where no NiO phase was detected [28,31]. Notably, in a related USY sample with the same Ni loading, namely USY-CH-Ni-oc-6 (20,000 ppm Ni), these absorption peaks are not detected. However, for a higher Ni-content sample (USY-CH-Ni-oc-7; 50,000 ppm Ni), the absorption peak at 718 nm can be observed. In the near IR region, NiO shows a broad absorption centered at 1119 nm, attributed to the  ${}^3A_{2g} \rightarrow {}^3T_{2g}$  d-d transition of  $\text{Ni}^{2+}$ . This absorption is shifted to 987 nm in the  $\text{Al}_2\text{O}_3$ -CH-Ni-oc-6 (20,000 ppm Ni), due to the “isolated” nature of  $\text{Ni}^{2+}$  species inside the  $\text{Al}_2\text{O}_3$  matrix. Representative spectra of Ni-loaded FCC catalysts with 10,000 ppm Ni (BLB-CAT-4 and BLF-CAT-4) are also shown in Figure 11 in comparison with the corresponding spectrum of NiO. In both catalysts, no peak associated with the NiO phase could be detected; however, a relatively broad shoulder centered at 575 nm could be attributed to the presence of “isolated”  $\text{Ni}^{2+}$ , in accordance with the data presented above for sample  $\text{Al}_2\text{O}_3$ -CH-Ni-oc-6. Although in the PXRD patterns of both samples, the (2 0 0) reflection of the NiO (bunsenite) structure was clearly visible (Figures 7 and 8), the presence of NiO could not be verified by the UV-vis analysis.



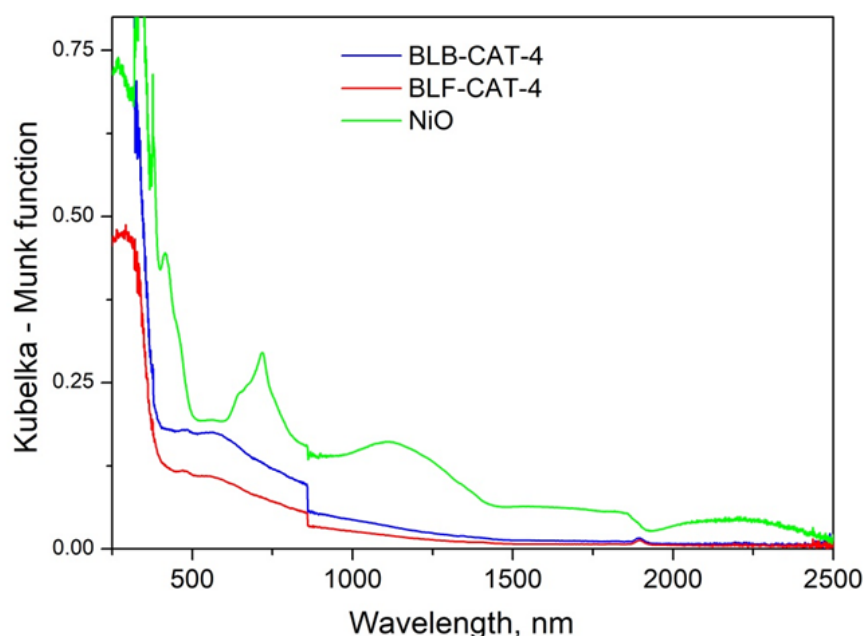


**Figure 11.** UV-Vis near IR diffuse reflectance spectra of representative Ni-impregnated materials: SiO<sub>2</sub>-CH-Ni-oc-6 (2 wt.% Ni), Al<sub>2</sub>O<sub>3</sub>-CH-Ni-oc-6 (2 wt.% Ni), USY-CH-Ni-oc-6 and 7 (2 and 5 wt.% Ni), and FCC catalysts BLF-CAT-4 and BLB-CAT-4 with 1 wt.% Ni. The spectra of bulk NiO and NiAl<sub>2</sub>O<sub>4</sub>/NiO are also included for comparison.

### 3.5. Raman Spectroscopy

Raman spectra of representative Ni-impregnated SiO<sub>2</sub> and Al<sub>2</sub>O<sub>3</sub> materials, as well as of the bulk NiO sample are shown in Figure 12. The spectrum of NiO exhibits a high intensity band at  $\sim 505\text{ cm}^{-1}$  with a shoulder at  $\sim 400\text{ cm}^{-1}$ , and a smaller band at  $\sim 1080\text{ cm}^{-1}$  attributed to the first-order longitudinal optical (LO) and 2LO phonon modes of NiO, respectively, in accordance with the literature [43–45]. The high intensity band of NiO can also be easily identified in the SiO<sub>2</sub>-CH-Ni-oc-3 (5000 ppm Ni) sample, shifted however, to higher frequencies at  $\sim 540\text{ cm}^{-1}$ , possibly due to substantial smaller crystal size (at the nanometer scale) of the highly dispersed NiO on the surface of SiO<sub>2</sub> compared with the larger crystals of bulk NiO, as revealed by the relevant XRD patterns [46]. Furthermore, possible interactions of Ni with the surface oxygen atoms of SiO<sub>2</sub> may impose additional effects resulting in the observed Raman band shift. This band is clearly visible (at  $\sim 545\text{ cm}^{-1}$ ) in the spectrum of the high Ni-content Al<sub>2</sub>O<sub>3</sub>-CH-Ni-oc-8 (200,000 ppm Ni) sample. The low intensity band at  $\sim 389\text{ cm}^{-1}$  in the spectrum of this high-Ni sample is attributed to NiAl<sub>2</sub>O<sub>4</sub>, in accordance with literature data [47] and the Raman spectrum of the reference bulk NiAl<sub>2</sub>O<sub>4</sub>/NiO sample (shown also in Figure 12). These data are in accordance with the PXRD results of sample Al<sub>2</sub>O<sub>3</sub>-CH-Ni-oc-8 (Figure 6), which clearly showed the presence of a distinct NiO crystalline phase but not of a well-defined crystalline NiAl<sub>2</sub>O<sub>4</sub> phase (only a shift to lower  $2\theta$  values of Al<sub>2</sub>O<sub>3</sub> reflections was observed, indicating the insertion of Ni<sup>2+</sup> in its lattice).

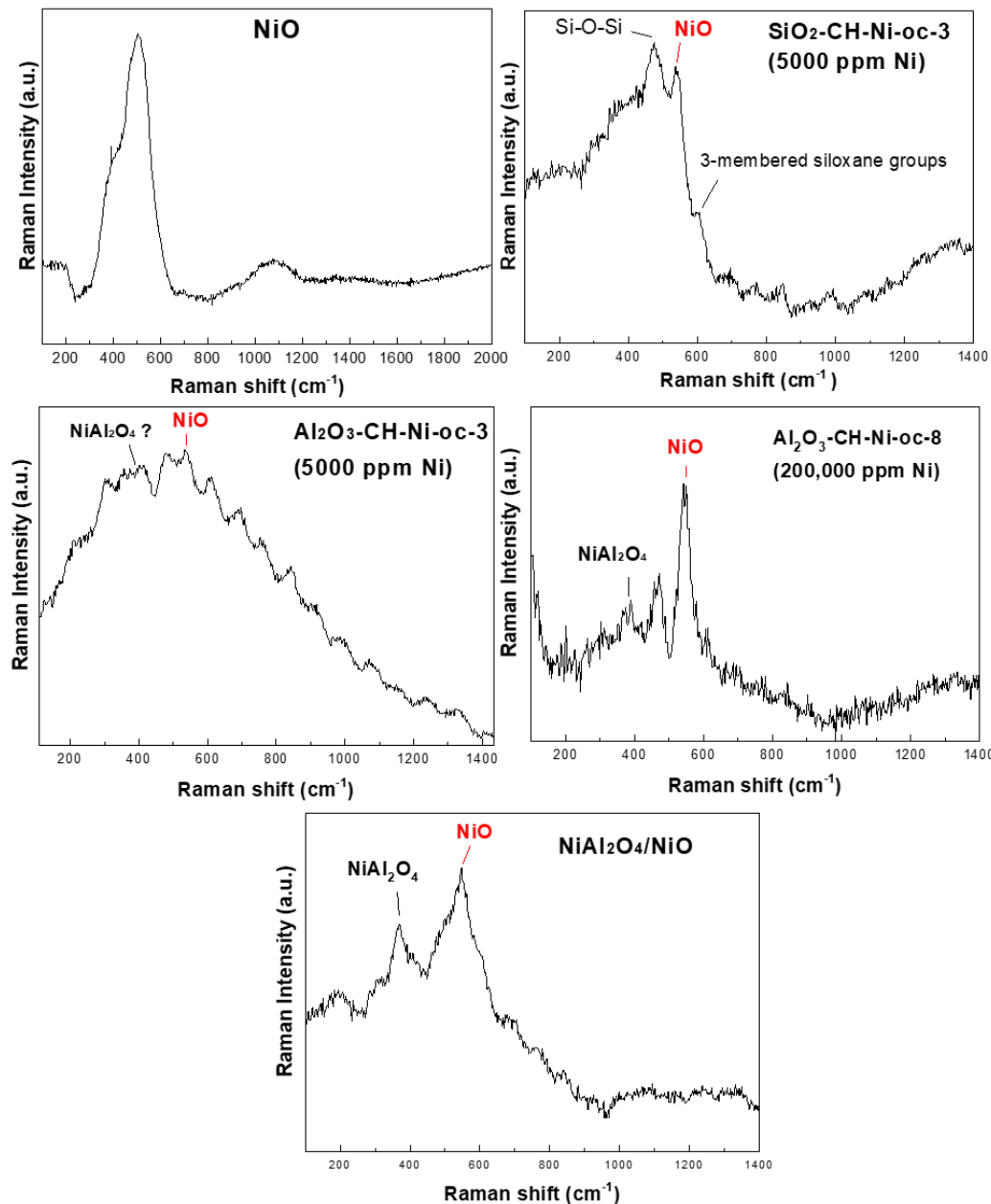


**Figure 12.** Raman spectra of bulk NiO and NiAl<sub>2</sub>O<sub>4</sub>/NiO and of representative Ni-impregnated SiO<sub>2</sub> and Al<sub>2</sub>O<sub>3</sub> materials: SiO<sub>2</sub>-CH-Ni-oc-3 (5000 ppm Ni), Al<sub>2</sub>O<sub>3</sub>-CH-Ni-oc-3 (5000 ppm Ni) and Al<sub>2</sub>O<sub>3</sub>-CH-Ni-oc-8 (200,000 ppm Ni).

The Raman spectra of representative Ni-loaded FCC catalysts and equilibrium FCC catalysts (Ecats) are shown in Figures 13 and 14, respectively. The characteristic band of NiO can be hardly identified in any Ni-loaded FCC catalysts at  $\sim 540\text{--}544\text{ cm}^{-1}$ , despite the relatively high Ni content, especially of BLF-CAT-4 and BLB-CAT-4 having 10,000 ppm Ni—compared to Al<sub>2</sub>O<sub>3</sub>-CH-Ni-oc-3 (5000 ppm Ni) for which a clearer Raman peak was observed (Figure 12). Furthermore, both BLF-CAT-4 and BLB-CAT-4 contain crystalline NiO (bunsenite) phases, as found by pxd, at the level of 1391 and 722 ppm Ni (or 1770 and 919 ppm NiO), respectively (Table 2), but still a well-resolved Raman band cannot be observed. One possible reason for this could be the presence of a relatively high content of TiO<sub>2</sub> (anatase) whose characteristic Raman bands are at  $\sim 140, 395, 510$  and  $630\text{ cm}^{-1}$  [48], the one at  $510\text{ cm}^{-1}$  being partially overlapped with the band of NiO. Similarly, the NiO band in the spectra of the Ecat samples B-CAT-5M and B-CAT-6M is very weak since both

contain low portions of the NiO phase (191 and 442 ppm NiO, PXRD data, Table 2), despite the relatively high total Ni content of B-CAT-5M (5141 ppm Ni).

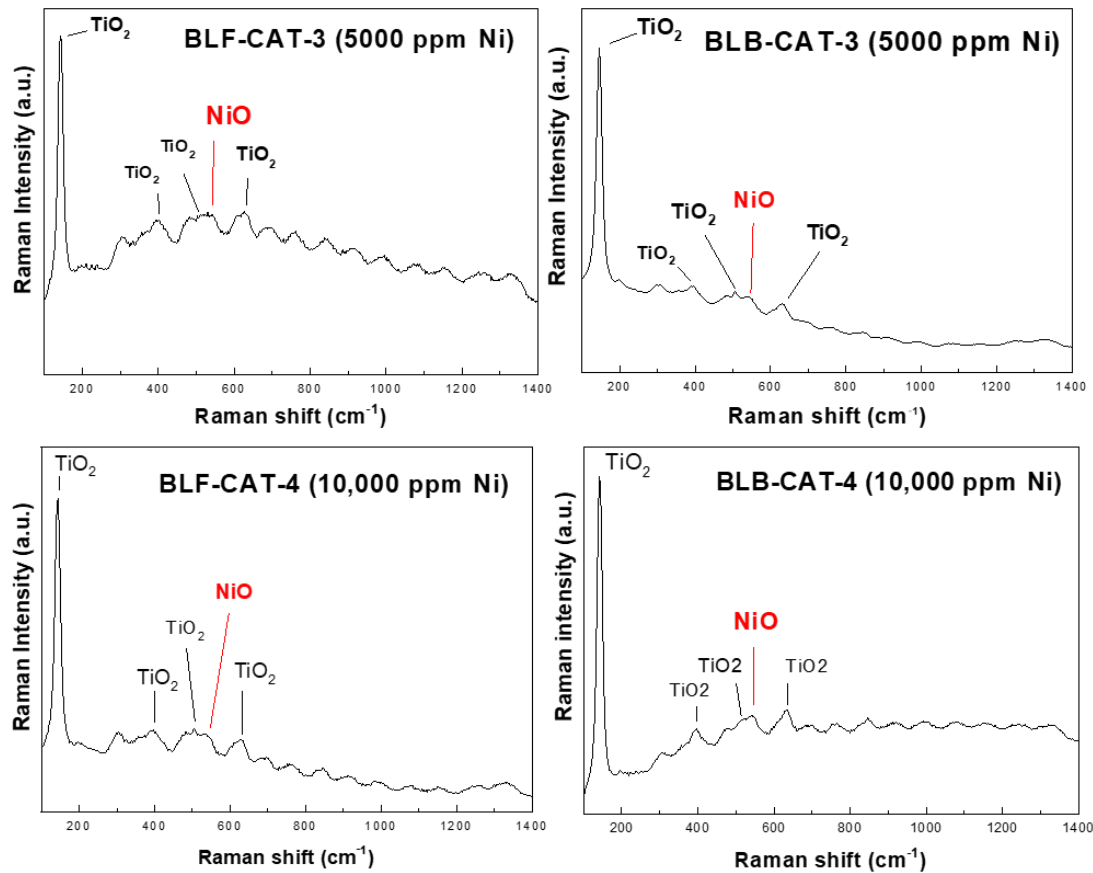


**Figure 13.** Raman spectra of Ni-loaded FCC catalysts: BLF-CAT-3 and BLB-CAT-3 (also containing boron) with 5000 ppm Ni, and BLF-CAT-4 and BLB-CAT-4 (also containing boron) with 10,000 ppm Ni.

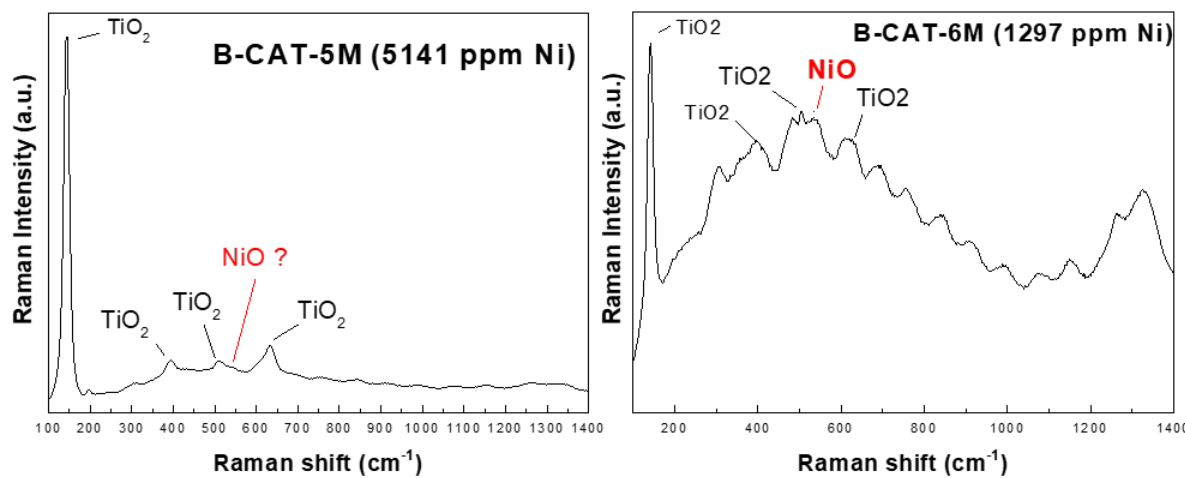


**Figure 14.** Raman spectra of equilibrium FCC catalysts (Ecats): B-CAT-5M (5141 ppm Ni) and B-CAT-6M (1297 ppm Ni).

### 3.6. X-ray Photoelectron Spectroscopy (XPS)

X-ray photoelectron spectroscopy (XPS) was used to provide information about the oxidation state and the chemical environment of nickel surface species, especially regarding their interaction with alumina. The Ni 2p XP spectra of representative Ni-impregnated  $\text{SiO}_2$ ,  $\text{Al}_2\text{O}_3$  and USY zeolite samples are shown in Figure 15. The XP spectra of representative Ni-loaded FCC and equilibrium catalysts are shown in Figure 16. The Ni 2p spectra of NiO supported on pure  $\text{SiO}_2$  (sample  $\text{SiO}_2\text{-CH-Ni-oc-6}$ ; 20,000 ppm Ni) exhibits a main peak in the  $2p_{3/2}$  region at the binding energy of 854.7 eV along with a shake-up satellite at ~860.2 eV, in accordance with the values reported for bulk NiO [28,49,50]. The shoulder at ~857 eV can be ascribed either to the second peak of the doublet peak usually observed in the  $2p_{3/2}$  core-level photoemission spectra of NiO [28,31,50,51] or to the  $\text{Ni(OH)}_2$  phase [50,52]. The shoulder at ~852.3 eV has been previously assigned to the Ni(0) metallic phase [50,53].

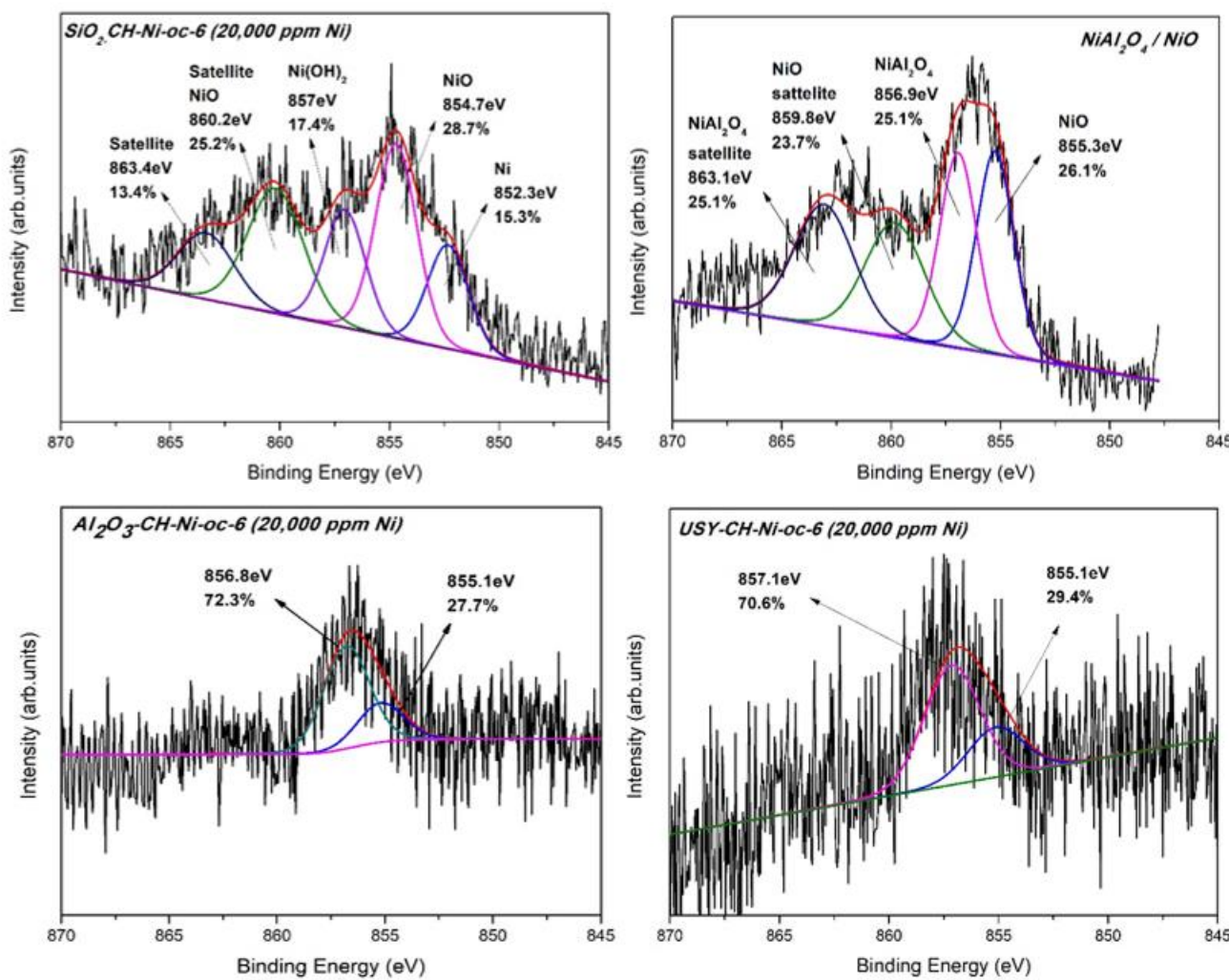


**Figure 15.** XPS spectra of the Ni  $2p_{3/2}$  region of representative Ni-impregnated  $\text{SiO}_2$ ,  $\text{Al}_2\text{O}_3$  and USY zeolite materials:  $\text{SiO}_2\text{-CH-Ni-oc-6}$  (20,000 ppm Ni),  $\text{Al}_2\text{O}_3\text{-CH-Ni-oc-6}$  (20,000 ppm Ni) and  $\text{USY-CH-Ni-oc-6}$  (20,000 ppm Ni). The spectrum of bulk  $\text{NiAl}_2\text{O}_4/\text{NiO}$  is also included for comparison.

The main XPS peak in the Ni  $2p_{3/2}$  region of the sample  $\text{NiAl}_2\text{O}_4/\text{NiO}$  can be deconvoluted in two clearly resolved components: one at 855.3 eV assigned to NiO and one at 856.9 eV that is attributed to  $\text{Ni}^{2+}$  in  $\text{NiAl}_2\text{O}_4$  phases [28,49]. The peaks at 859.8 eV and 863.1 eV correspond to the shake-up satellites of the above peaks, respectively. The Ni 2p XP spectra of the samples  $\text{Al}_2\text{O}_3\text{-CH-Ni-oc-6}$  (20,000 ppm Ni) and  $\text{USY-CH-Ni-oc-6}$  (20,000

ppm Ni) are similar, exhibiting a low intensity peak due to the relatively low total content of Ni, which is deconvoluted in two components: the strongest one is assigned to the  $\text{NiAl}_2\text{O}_4$  phase (~70%) and the weakest one is attributed to  $\text{NiO}$  (~30%) (as can be seen in Figure 15). It is thus obvious that XPS can identify the presence of  $\text{NiO}$  phases in the  $\text{Al}_2\text{O}_3$  and USY impregnated samples, as well as of  $\text{Ni}^{2+}$  related to  $\text{NiAl}_2\text{O}_4$ , at the level of 20,000 ppm total Ni, although no reflections of  $\text{NiO}$  or  $\text{NiAl}_2\text{O}_4$  were observed in their prxd patterns (Figures 6 and Figure S1, respectively). In the case of the FCC catalysts loaded with 10,000 ppm Ni, despite the low signal to noise ratio, a peak in the  $\text{Ni } 2\text{p}_{3/2}$  region can be also identified and is deconvoluted in two peaks, i.e., ~55% assigned to the  $\text{NiAl}_2\text{O}_4$  phase and ~45% to  $\text{NiO}$ , with no clear differentiation between the boron-containing (BLB-CAT-4) and the boron-free (BLF-CAT-4) samples (Figure 16). Relatively higher  $\text{NiAl}_2\text{O}_4/\text{NiO}$  ratios (ca. ≥80%) have been reported for Ecats with similar total Ni contents [8]. In the case of the Ecats of the present study, no clear signals attributed to  $\text{NiO}$  or  $\text{NiAl}_2\text{O}_4$  phases could be identified.

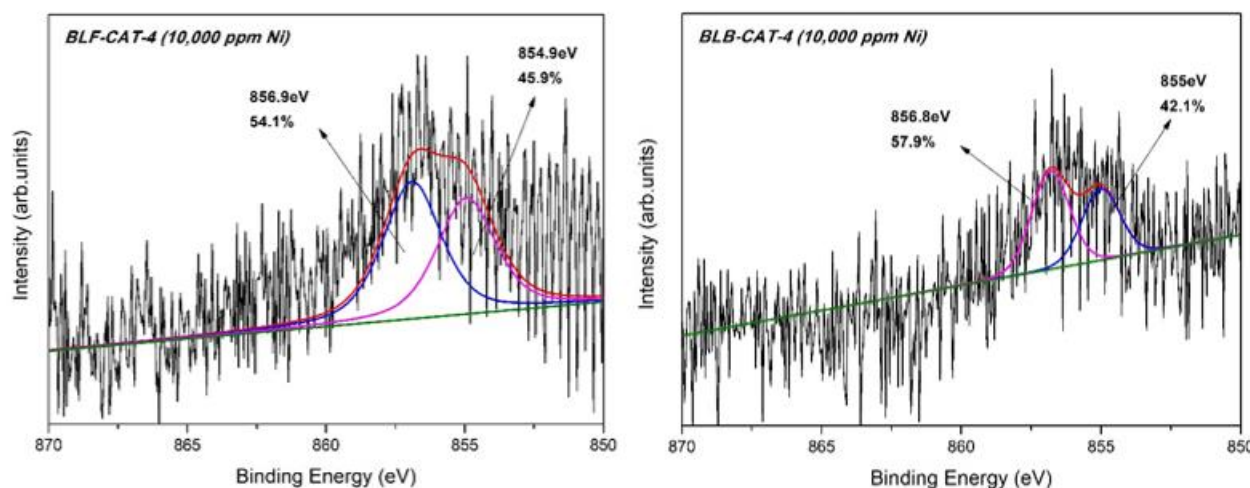


**Figure 16.** XPS spectra of the  $\text{Ni } 2\text{p}_{3/2}$  region of Ni-loaded FCC catalysts: BLF-CAT-4 and BLB-CAT-4 (also containing boron) with 10,000 ppm Ni.

### 3.7. Scanning Electron Microscopy—Energy Dispersive Spectroscopy (SEM-EDS)

The morphological characteristics of representative Ni-impregnated samples and equilibrium FCC catalysts (Ecats) were studied by SEM imaging at various magnifications, and micro-analysis data were obtained by spot-EDS measurements as well as EDS mapping on flat cross-sections of the catalyst's particles (see the Experimental section for details).

#### SEM images and point EDS microanalysis

Representative SEM images and point EDS analysis data of Ni-loaded FCC catalysts and equilibrium catalysts (Ecats) are shown in Figures S3–S6 (Supplementary Material). The comparison of the SEM images of the Ni-loaded lab-deactivated FCC catalysts (BLF and BLB series) with those of the Ecats (B-CAT-2M and 5M) did not reveal any significant morphology differences. The point EDS microanalysis data are indicative (based on 3–6 points data) of the chemical composition of each catalyst as well as of the relative (in)homogeneity of the particles, as expected for these types of complex catalyst formulations.

#### EDS elemental mapping of flat cross-sections

Elemental mapping images along with the EDS microanalysis data for representative Ni-impregnated  $\text{SiO}_2$ ,  $\text{Al}_2\text{O}_3$  and USY samples, as well as Ni-loaded FCC catalysts and

equilibrium catalysts (Ecats), are shown in Figures 17–19 and Figures S7–S10 (Supplementary Material).

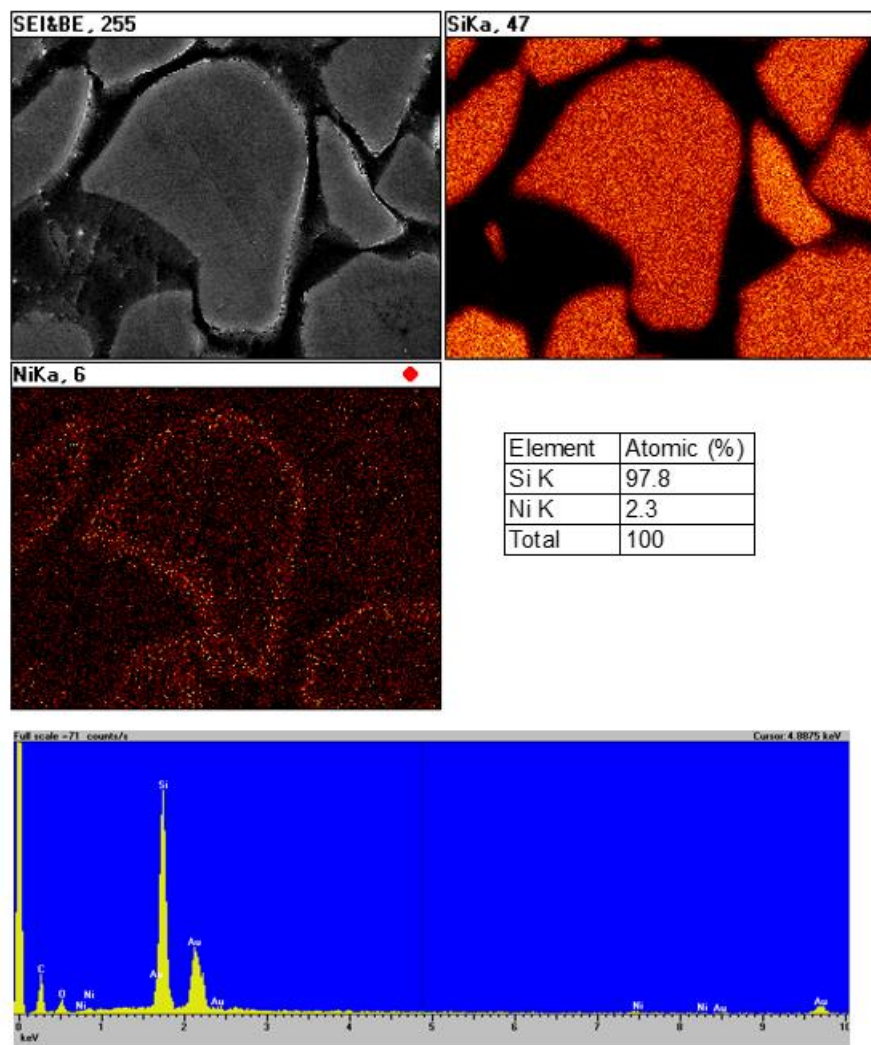


**Figure 17.** SEM image and EDS elemental mapping of representative Ni-impregnated  $\text{SiO}_2$  sample:  $\text{SiO}_2\text{-CH-Ni-oc-4}$  (10,000 ppm Ni).

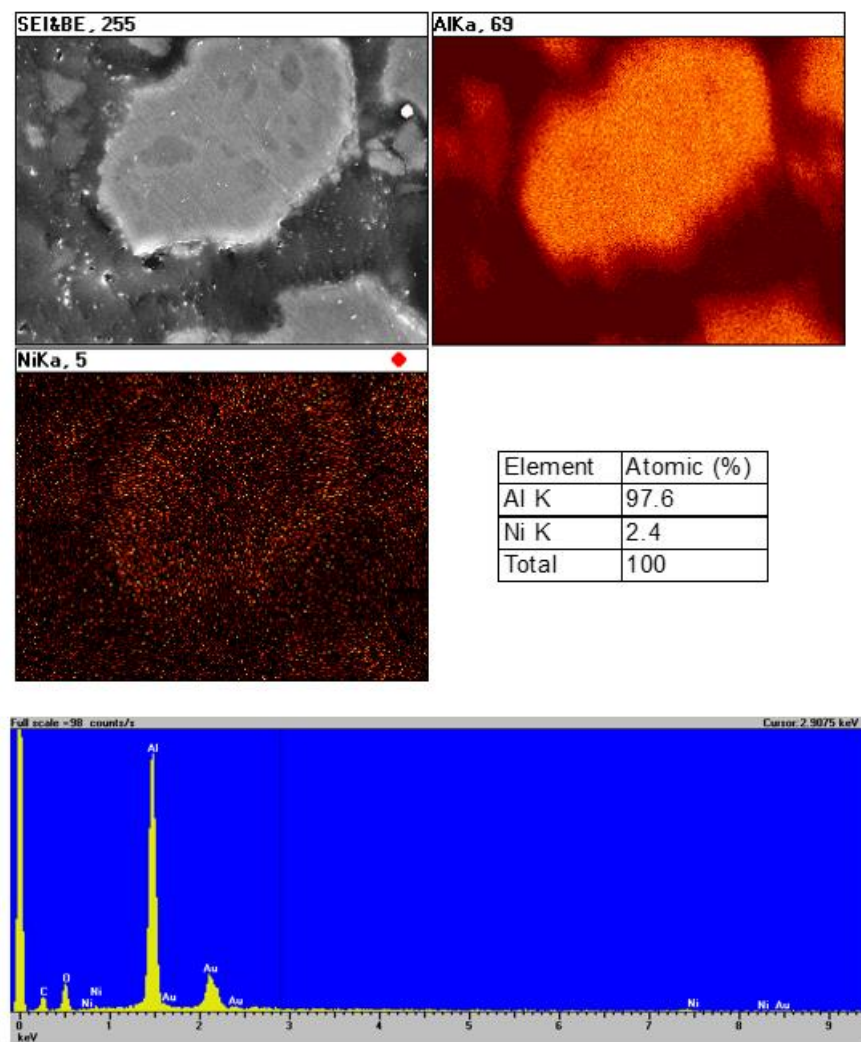


**Figure 18.** SEM image and EDS elemental mapping of representative Ni-impregnated  $\text{Al}_2\text{O}_3$  sample:  $\text{Al}_2\text{O}_3\text{-CH-Ni-oc-4}$  (10,000 ppm Ni).

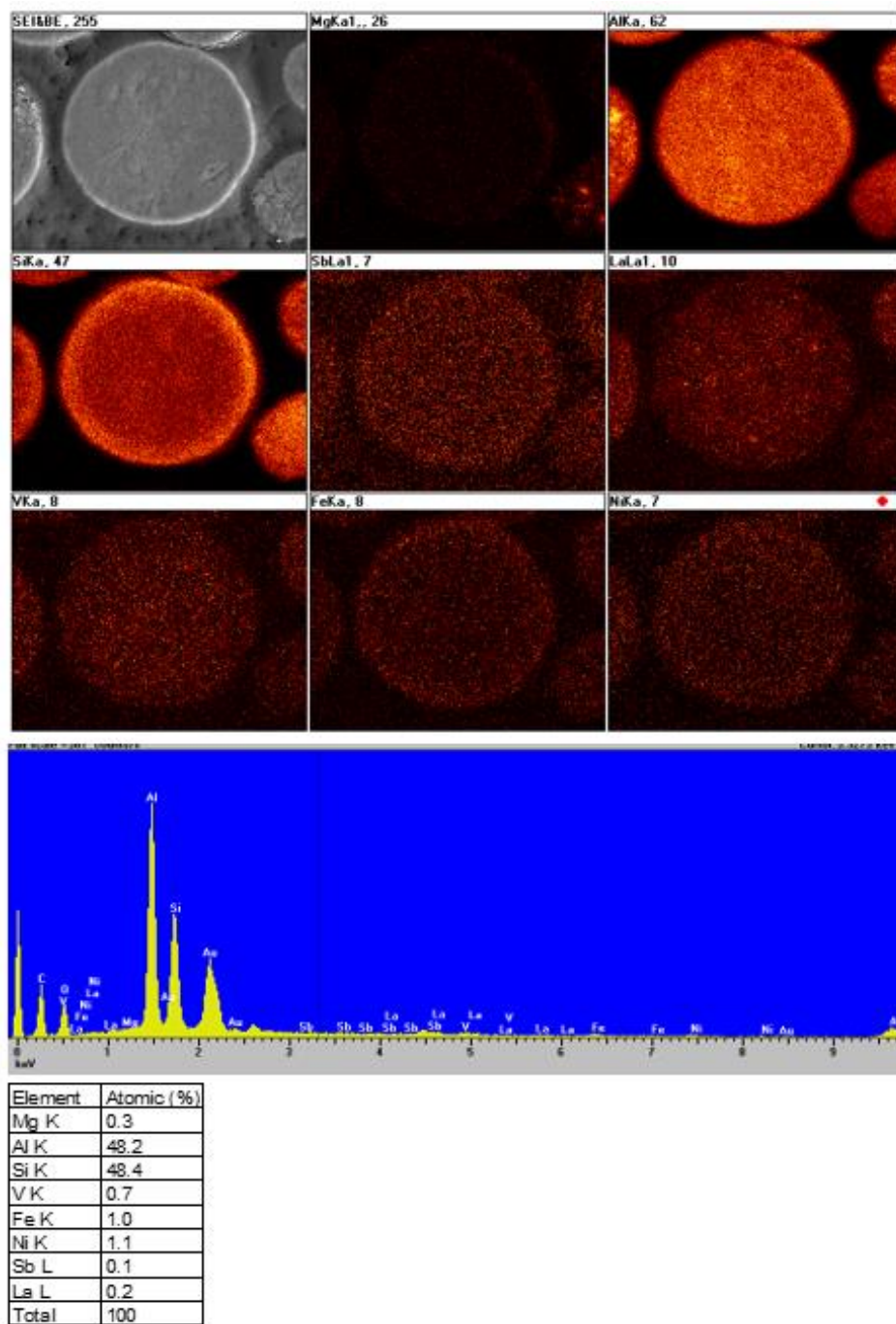


**Figure 19.** SEM image and EDS elemental mapping of equilibrium FCC catalyst: B-CAT-5M (5141 ppm Ni).

The elemental mapping of the Ni-impregnated (10,000 ppm) USY zeolite sample revealed a homogeneous distribution of Ni throughout the whole particle without any observable aggregates, whereas in the case of  $\text{SiO}_2$  and  $\text{Al}_2\text{O}_3$ , a slight enrichment of the particle periphery can be observed (Figure S7 and Figures 17 and 18). A uniform distribution of Ni without aggregated spots or increasing density in the periphery of the particles can be also observed for the two lab-prepared and deactivated Ni-loaded FCC catalysts, i.e., BLF-CAT-4 and BLB-CAT-4, both with 10,000 ppm Ni and the latter also containing boron. No difference between the two catalysts could be identified (Figures S8 and S9). With regard to the effect of the lab-deactivation method (i.e., the Mitchell method coupled with the CPS or CDU method) or type of Ni reagent (i.e., dendritic porphyrin or nickel

naphthenate), the reported results with respect to the distribution of Ni throughout the FCC particle are contradictory, depending also on the detection method used (i.e., SEM-EDS, XPS, etc.) [8,24,25].

Two representative equilibrium FCC catalysts with total Ni content in the range of ca. 4300 to 5140 ppm were examined (Figure 19 and S10), and they both exhibited a homogeneous Ni distribution, with an enhancement of Ni content in the periphery. Higher Ni concentration on the edge of the particles has been previously reported for Ecats with the use of Secondary Ion Mass Spectrometry (SIMS) [54], line-scanning SEM-EDS analysis [55] or very detailed point-EDS microanalysis across the particle cross-sections [25]. However, it was also shown that depending on the accessibility properties of the FCC particles, the distribution of Ni between the edge and the core of the particles of a high-accessibility catalyst do not differ significantly [24]. Furthermore, the deposition and distribution of Ni on Ecat particles might also be highly technology dependent, being related to the presence of specialty Ni trapping alumina at the catalyst particle and whether this specialty alumina is distributed evenly throughout the particle or concentrated at the outside [56].

### 3.8. Transmission Electron Microscopy (TEM)—High resolution TEM (HRTEM)

The nanoscale morphological and textural characteristics of representative Ni-imregnated  $\text{SiO}_2$ ,  $\text{Al}_2\text{O}_3$  and USY zeolite samples and of equilibrium FCC catalysts were studied by TEM and HRTEM. Furthermore, STEM/EDXS was employed in order to study the distribution of elements in the particles. Representative TEM/HRTEM images of the  $\text{SiO}_2$ ,  $\text{Al}_2\text{O}_3$  and USY zeolite samples impregnated with 1000, 2500 and 1000/10,000 ppm Ni, respectively, are shown in Figure 20. Extensive investigation on several particles of the above samples showed that Ni has been highly dispersed on these supports, almost at an atomic level, since the identification of well-formed Ni or  $\text{NiO}$  nanoparticles was not possible. Only in the case of the  $\text{SiO}_2$ -CH-Ni-oc-1 (1000 ppm Ni) could a few small nanoparticles of ca. 4–5 nm be spotted, as shown in Figure 20a. The amount/size of these were not sufficient to observe  $\text{NiO}$  reflections in the pxrd pattern (Figure 1). The lattice fringes can be clearly seen in the HRTEM image (Figure 20a), in which the interplanar distance is determined to be approximately 0.21 nm, and is fully consistent with the d-spacing of the (200) Bragg reflection of cubic  $\text{NiO}$ .

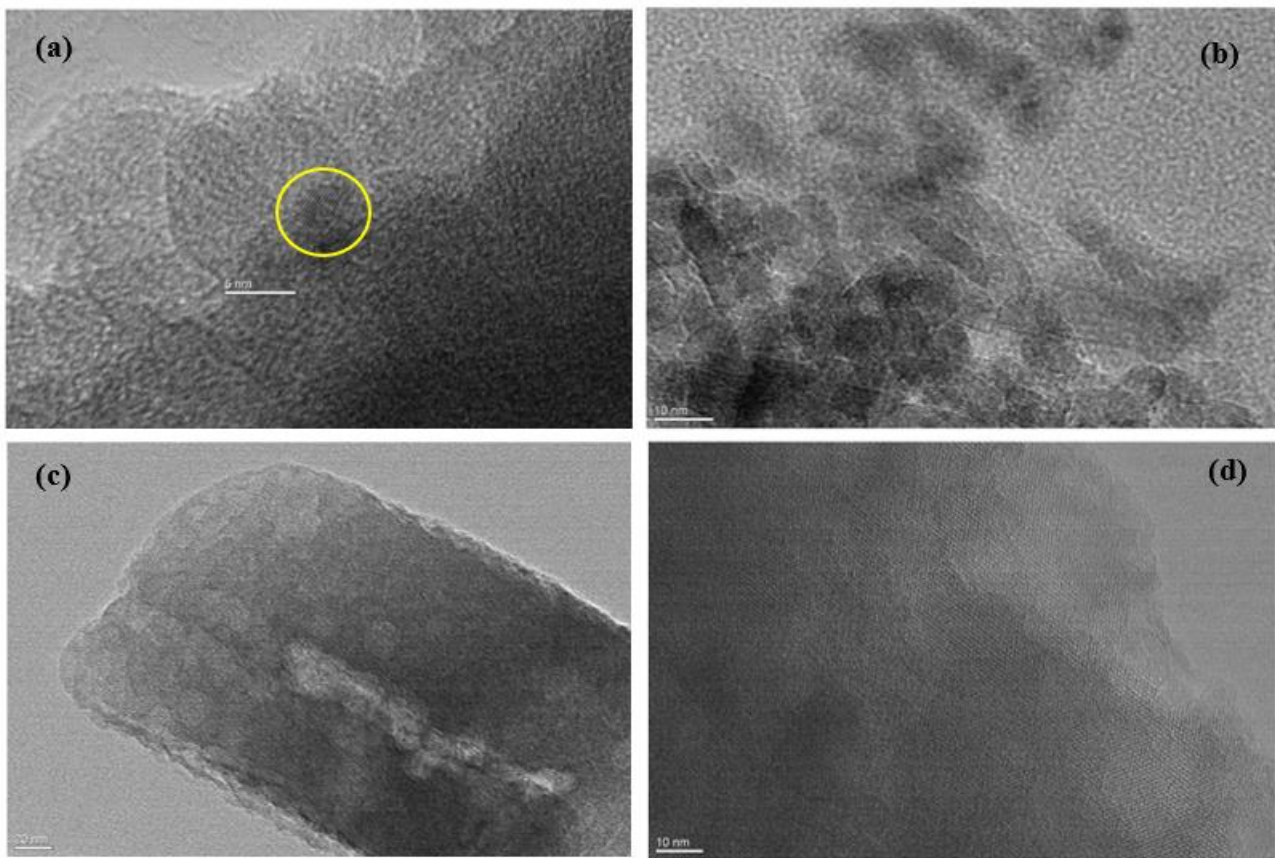


**Figure 20.** Representative TEM/HRTEM images of (a) SiO<sub>2</sub>-CH-Ni-oc-1 (1000 ppm Ni), (b) Al<sub>2</sub>O<sub>3</sub>-CH-Ni-oc-2 (2500 ppm Ni), (c) USY-CH-Ni-oc-1 (1000 ppm Ni), and (d) USY-CH-Ni-oc-4 (10,000 ppm Ni).

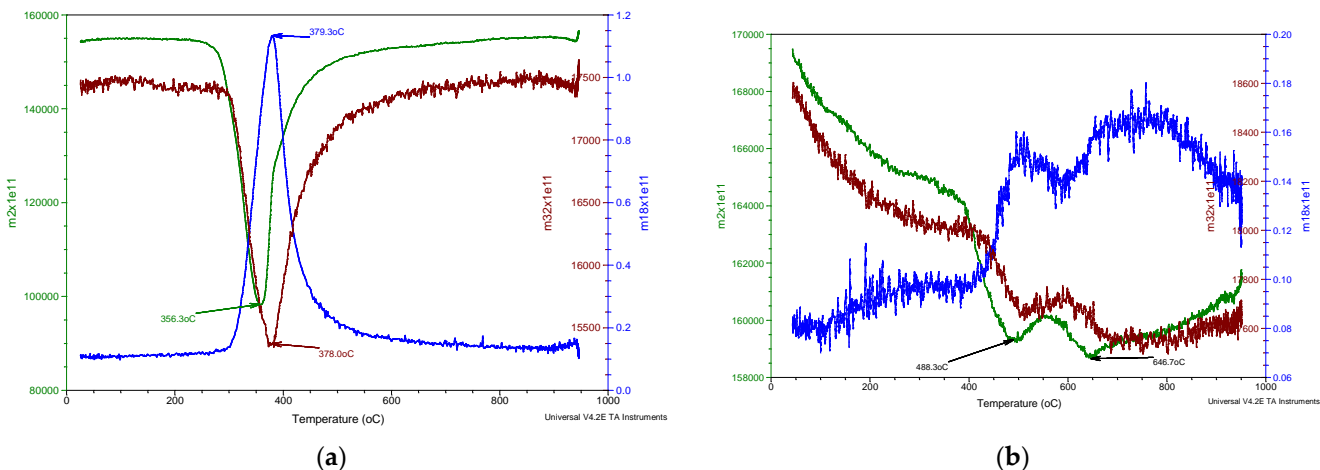
### 3.9. Temperature Programmed Reduction with H<sub>2</sub> (TPR-H<sub>2</sub>)

The reduction characteristics of bulk NiO and NiO/NiAl<sub>2</sub>O<sub>4</sub> phases formed on pure supports (i.e., SiO<sub>2</sub>, Al<sub>2</sub>O<sub>3</sub> and USY zeolite) and on Ni-loaded FCC catalysts, as well as on equilibrium FCC catalysts were studied by TPR-H<sub>2</sub>. As can be seen from Figure 21a, the TPR profile of bulk NiO exhibits a strong, relatively sharp peak with maximum at ~378 °C, in accordance with the literature [23,28,49]. However, the reduction profile of the Ni<sup>2+</sup> phases formed on SiO<sub>2</sub> after impregnation with Ni octanoate and calcination in air (sample SiO<sub>2</sub>-CH-Ni-oc-6 with 20,000 ppm Ni) exhibits two broad peaks with maxima at 488 and 647 °C (Figure 21b), which can be attributed to NiO nano-crystallites (low-temperature) and amorphous surface nickel silicate or hydroxysilicate (high-temperature), as previously reported [57]. The TPR-H<sub>2</sub> profile of the Al<sub>2</sub>O<sub>3</sub>-CH-Ni-oc-7 sample containing 100,000 ppm Ni (Figure 21c) shows two peaks, a weak broad one with max. at ~402 °C and a strong sharper one at ~786 °C that are attributed to a reduction of N<sup>2+</sup> in the NiO and NiAl<sub>2</sub>O<sub>4</sub> phases, respectively, despite the absence of any bulk NiO and NiAl<sub>2</sub>O<sub>4</sub>, as evidenced by pxrd (Figure 6). At higher Ni loadings, i.e., 200,000 ppm (or 20 wt.%), a more complex TPR profile is obtained, as can be seen in Figure S11 (Supplementary Material) for the sample Al<sub>2</sub>O<sub>3</sub>-CH-Ni-oc-8. The sharp and more intense peak with two distinct maxima at ~448 and 486 °C is attributed to NiO of different natures. The first maxima is probably related to the bulk crystalline NiO also identified by the pxrd measurements (Figure 6), and the second is related to a more dispersed NiO phase interacting more strongly with the Al<sub>2</sub>O<sub>3</sub> surface. A very broad and weak peak at ~652 °C may also be attributed to a NiO phase strongly bound to the support. The strong and sharp peak at ~832 °C is related to the reduction of Ni<sup>2+</sup> in the NiAl<sub>2</sub>O<sub>4</sub> phases which are still not well crystallized and capable to induce the respective reflections in the pxrd patterns (Figure 6). Similar TPR profiles

dividing the  $\text{Ni}^{2+}$  species into different types with regard to their nature and reducibility have been also previously reported [49]. The peak(s) located at the low temperature region of ca. 300–550 °C were assigned to free  $\text{NiO}$  species having weak interaction with the support. The peaks at intermediate temperatures of ca. 550–700 °C were attributed to  $\text{NiO}$  species with a stronger interaction with alumina, and the high-temperature peaks (>700 °C) were related to the stable nickel aluminate phase with a spinel structure. The TPR profile of the USY zeolite (Figure S12, Supplementary Material) sample containing 50,000 ppm Ni (USY-CH-Ni-oc-7) is more or less similar to that of  $\text{Al}_2\text{O}_3$ -CH-Ni-oc-7 (100,000 ppm Ni), exhibiting two peaks, including a weak broad peak with max. at ~365 °C and a strong sharper one at ~687 °C attributed to reduction of  $\text{N}^{2+}$  in  $\text{NiO}$  and  $\text{NiAl}_2\text{O}_4$  phases, respectively, despite the absence of any bulk  $\text{NiO}$  and  $\text{NiAl}_2\text{O}_4$ , as evidenced by pxrd (Figure S1, Supplementary Material).

The TPR-H<sub>2</sub> profiles of the two representative Ni-loaded lab-deactivated FCC catalysts, i.e., BLF-CAT-4 and BLB-CAT-4, both containing 10,000 ppm Ni, are shown in Figure 21d,e, respectively. For both samples, the TPR profiles exhibit the classical two peaks, a low-temperature very weak broad peak related to the  $\text{NiO}$  phases and a high temperature strong peak attributed to the reduction of  $\text{Ni}^{2+}$  in the  $\text{NiAl}_2\text{O}_4$  spinel phase. The high-temp peak is of similar shape and at similar temperature, ca. 860–866 °C, for both catalysts, while a noticeable difference can be seen at the low-temp peak, the peak of BLF-CAT-4 (with max. at ~374 °C) being more intense compared with that of the boron-containing counterpart BLB-CAT-4 (with max. at ~411 °C). This difference is indicative of the presence of higher amount of easily reducible bulk  $\text{NiO}$  in the former catalyst, in accordance with the PXRD data presented in Table 2. This observation is in agreement with a previous report on the inhibited reducibility of Ni in catalysts from BBT technology [27].

The TPR-H<sub>2</sub> profile of a representative equilibrium FCC catalyst, B-CAT-5M, containing 5141 ppm Ni is shown in Figure 21f. Its profile is slightly different compared with those of the lab-prepared FCC catalysts, i.e., a low-temp peak attributed to the easily reducible bulk  $\text{NiO}$  can also be seen but at a relatively lower temperature, i.e., 279 °C, in addition to a very weak peak at ~530 °C. Furthermore, the high-temp peak, with a maximum at ~862 °C is still very intense. This is indicative of the presence of not easily reducible  $\text{Ni}^{2+}$  species, mostly in  $\text{NiAl}_2\text{O}_4$  related phases, with a clear benefit for the FCC process since the formation of the undesirable  $\text{Ni}(0)$  species is inhibited. Previous works have shown the peak at ~525 °C being dominant with that at ~820 °C being of lower intensity [23].



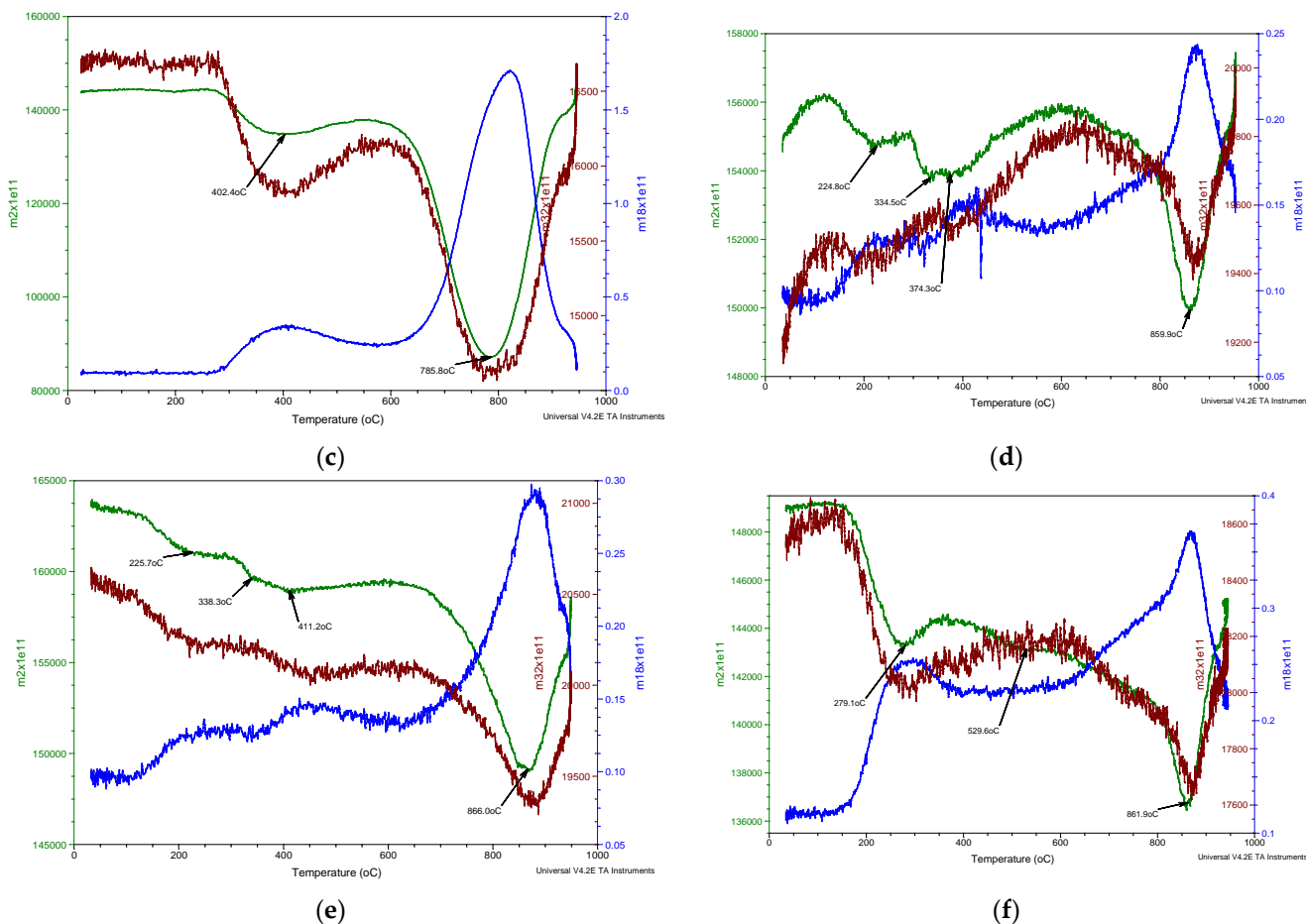


**Figure 21.** (a) TPR-H<sub>2</sub> profile of bulk NiO (diluted in SiO<sub>2</sub> by physical mixing, 5 wt.% NiO). (b) TPR-H<sub>2</sub> profile of SiO<sub>2</sub>-CH-Ni-oc-6 sample containing 20,000 ppm Ni. (c) TPR-H<sub>2</sub> profile of Al<sub>2</sub>O<sub>3</sub>-CH-Ni-oc-7 sample containing 100,000 ppm Ni. (d) TPR-H<sub>2</sub> profile of the Ni-loaded FCC catalyst BLF-CAT-4 containing 10,000 ppm Ni. (e) TPR-H<sub>2</sub> profile of the Ni-loaded FCC catalyst BLB-CAT-4 with 10,000 ppm Ni (containing also boron). (f) TPR-H<sub>2</sub> profile of the equilibrium FCC catalyst B-CAT-5M with 5141 ppm Ni.

#### 4. Conclusions and Outlook

The main objective of this contribution was the qualitative and quantitative identification of the various phases of Ni, mainly as NiO or NiAl<sub>2</sub>O<sub>4</sub> spinel phases that are usually present in equilibrium Fluid Catalytic Cracking (FCC) catalysts (Ecats). The investigation was based on detailed analysis and a combination of experimental data obtained by systematic physicochemical characterization of prototype Ni-impregnated SiO<sub>2</sub>, Al<sub>2</sub>O<sub>3</sub> and USY zeolite samples, Ni-impregnated and lab-deactivated FCC samples, and equilibrium FCC catalysts obtained from different refineries, using a series of techniques, including XRF, ICP-AES, PXRD, FT-IR, UV-Vis-NIR, SEM-EDS, TEM/HRTEM, XPS, RAMAN and TPR-H<sub>2</sub>.

It was shown that the PXRD method is capable of detecting bulk NiO at very low (ca. 1000 ppm NiO or 786 ppm Ni) concentrations in solid mixtures, but higher Ni loadings (ca.  $\geq$ 2500 ppm) are required when NiO is highly dispersed and/or not well-crystallized over porous supports such as SiO<sub>2</sub> and FCC catalysts. For pure Al<sub>2</sub>O<sub>3</sub> or USY zeolite catalysts, even higher Ni loadings are required in order for NiO to become “visible”, i.e.,  $\geq$ 10 and 5 wt.%, respectively. Furthermore, the relatively limited interaction of Ni with SiO<sub>2</sub> and the absence of any other reflections, except those of NiO (bunsenite) in the Ni-impregnated/calculated SiO<sub>2</sub> samples, allowed for the construction of calibration lines correlating the total NiO content with the integrated peak area of the (2 0 0) reflection of NiO (bunsenite) at  $\sim$ 43.3° 2θ. This approach is “sensitive” to various parameters, such as the Ni/SiO<sub>2</sub>

impregnation-preparation method (which affects initial deposition of the Ni(oxy)hydroxide species and subsequent NiO crystal nucleation and growth) and temperature (in general conditions) of calcination. Of course, it is also “sensitive” to accuracy in the analysis of Ni content, the application of slow scan high quality PXRD measurements and the accuracy in peak fitting-area integration of the NiO reflections.

For example, at least for the conditions used in the present study, the Ni/SiO<sub>2</sub> samples prepared via classical incipient wetness with aqueous solutions of Ni(NO<sub>3</sub>)<sub>2</sub> followed by drying and calcination in air for 3 h, provided a calibration line with higher slope compared with the line derived from the samples prepared via impregnation with Ni octanoate solution (diluted in cyclohexane) using SiO<sub>2</sub> supports that had been previously impregnated to incipient wetness with cyclohexane. We consider the latter case as more representative of the Ni deposition process during the FCC operation. However, if one uses, the calibration line of the Ni(NO<sub>3</sub>)<sub>2</sub> impregnated samples, erroneously lower NiO content values are estimated for the same PXRD integrated peak areas.

Based on the analysis of Ni-loaded FCC samples prepared by the Mitchell method and artificially deactivated by CPS, boron-based technology hindered the formation of the PXRD-detectable NiO (bunsenite) phase to almost half, compared with the non-boron counterpart catalyst, for the 10,000 ppm Ni addition level. This is a strong indication that the presence of boron has a measurable (based on PXRD) effect on passivating Ni, not allowing the formation of bulk nano-crystalline NiO. It was also shown by PXRD that for total Ni content of even above 5000 ppm in the equilibrium FCC catalysts from different refineries, the FCC catalysts containing Ni passivation technologies could minimize the formation of NiO phase to levels significant below the 0.1 wt% level, and therefore, the Equilibrium FCC catalysts cannot be classified as “hazardous waste”.

PXRD reflections due to bulk NiAl<sub>2</sub>O<sub>4</sub> could not be observed in any of the prototype or FCC catalysts. A peak shift of the characteristic reflections of Al<sub>2</sub>O<sub>3</sub>, (4 0 0) and (4 4 0), towards lower angles that was identified for the prototype Ni/Al<sub>2</sub>O<sub>3</sub> samples containing ≥5000 ppm Ni could not be observed for the FCC catalysts. FTIR bands attributed to NiO or NiAl<sub>2</sub>O<sub>4</sub> phases could not be easily observed in the Ni-loaded FCC catalysts or the Ecats, due to overlapping with zeolite or silica bands. UV-Vis-near IR spectra are also not useful for identifying low contents of NiO, such as those usually present in Ecats, i.e., ≤10,000 ppm Ni.

On the other hand, Raman spectroscopy is more sensitive to NiO and NiAl<sub>2</sub>O<sub>4</sub> phases, and the characteristic NiO band at ~537 cm<sup>-1</sup> could be observed even at the level of 5000 ppm Ni on pure Al<sub>2</sub>O<sub>3</sub>, despite of the absence of any NiO reflections in its PXRD pattern. NiAl<sub>2</sub>O<sub>4</sub> associated with the band at ~389 cm<sup>-1</sup> became clearly visible at relatively higher concentrations. XPS analysis could easily distinguish between N<sup>2+</sup> present in the NiO or NiAl<sub>2</sub>O<sub>4</sub> phases, as well as other possible oxidation states of Ni, and provide a relative ratio between these phases. However, for Ni levels below ca. 10,000 ppm the relevant XP signals become weak, and there is a high degree of uncertainty in the peak deconvolution procedure. Furthermore, XPS being a surface characterization method, is not capable of providing information on the bulk FCC particles.

TEM/HRTEM is a valuable tool for the identification of single or polycrystalline NiO nano-particles down to the level of few nanometers whose density is not sufficient to induce the typical PXRD reflections of the NiO (bunsenite) phase. However, in the presence of various other metals/oxides, such as La<sub>2</sub>O<sub>3</sub>, TiO<sub>2</sub>, Fe<sub>2</sub>O<sub>3</sub>, V<sub>2</sub>O<sub>5</sub>, etc. in the real FCC catalyst, it may become difficult to identify the NiO nanoparticles, especially when their lattice fringes are overlapped with those of the zeolite component, for example. Certainly, HRTEM can show the presence of individual highly dispersed NiO nanoparticles but cannot offer a quantitative analysis tool for classifying the equilibrium FCC catalysts.

TPR-H<sub>2</sub> is a very useful method for determining the reducibility of the various NiO/NiAl<sub>2</sub>O<sub>4</sub> phases on the FCC catalysts, thus providing indications of the nature of the Ni<sup>2+</sup> species, the strength of interaction with the support, and ultimately their “resistance” towards reduction to Ni(0) in the FCC riser. When comparing conventional vs. boron-

based technology catalysts, a noticeable difference can be observed at the low-temp peak, which is more intense for the conventional catalyst than the boron-containing counterpart. This difference is indicative of the presence of higher amount of easily reducible bulk NiO in the former catalyst, in accordance with the PXRD results.

Overall, the results of this study have shown the strengths and the weaknesses of relevant analytical techniques towards the accurate qualitative and quantitative identification of the various phases of Ni present in equilibrium FCC catalysts. A comparison of conventional versus boron-based Ni-passivation was presented. It was shown that catalysts from boron-based technology (BBT) demonstrate advanced Ni trapping capabilities by reducing the formation of NiO (PXRD) while keeping Ni at a less-reducible state (TPR-H<sub>2</sub>), thereby effectively hindering the deleterious Ni role in FCC operation.

**Supplementary Materials:** The following supporting information can be downloaded at: <https://www.mdpi.com/article/10.3390/catal13010003/s1>; Figure S1: (a) PXRD patterns of USY-CH-Ni-oc-X samples, prepared via impregnation of USY zeolite with Ni octanoate solution diluted in cyclohexane (see experimental section); X : (3) 5000 ppm Ni, (6) 20,000 ppm Ni, (7) 50,000 ppm Ni, and (b) Enlarged view in the range 35–70° 2θ. The patterns of NiO (blue pattern) and NiAl<sub>2</sub>O<sub>4</sub> (red pattern) are also shown for comparison.; Figure S2: FTIR spectra of representative Ni-impregnated materials: SiO<sub>2</sub>-CH-Ni-oc-5 (1.5 wt.% Ni), Al<sub>2</sub>O<sub>3</sub>-CH-Ni-oc-7 (10 wt.% Ni), USY-CH-Ni-oc-6 (2 wt.% Ni). The spectra of bulk NiO, NiAl<sub>2</sub>O<sub>4</sub>/NiO, silica gel, γ-Al<sub>2</sub>O<sub>3</sub> and USY zeolite, are also included for comparison; Figure S3: Representative SEM images and point EDS microanalysis data of Ni-loaded FCC catalyst: BLF-CAT-4 with 10,000 ppm Ni; Figure S4: Representative SEM images and point EDS microanalysis data of Ni-loaded FCC catalyst: BLB-CAT-4 (containing also boron) with 10,000 ppm Ni; Figure S5: Representative SEM images and point EDS microanalysis data of equilibrium FCC catalyst: B-CAT-2M (4327 ppm Ni); Figure S6: Representative SEM images and point EDS microanalysis data of equilibrium FCC catalyst: B-CAT-5M (5141 ppm Ni); Figure S7: SEM image and EDS elemental mapping of representative Ni-impregnated USY zeolite sample: USY-CH-Ni-oc-4 (10,000 ppm Ni); Figure S8: SEM image and EDS elemental mapping of representative Ni-loaded FCC catalyst: BLF-CAT-4 with 10,000 ppm Ni; Figure S9: SEM image and EDS elemental mapping of representative Ni-loaded FCC catalyst: BLB-CAT-4 (containing boron) with 10,000 ppm Ni; Figure S10: SEM image and EDS elemental mapping of equilibrium FCC catalyst: B-CAT-2M (4327 ppm Ni); Figure S11: TPR-H<sub>2</sub> profile of Al<sub>2</sub>O<sub>3</sub>-CH-Ni-oc-7 sample containing 200,000 ppm Ni; Figure S12: TPR-H<sub>2</sub> profile of USY-CH-Ni-oc-7 sample containing 50,000 ppm Ni;

**Author Contributions:** Conceptualization, K.S.T., V.K. and B.Y.; methodology, K.S.T., I.D.C. and P.N.T.; investigation, I.D.C., K.S.T. and P.T.; resources, K.S.T., V.K. and B.Y.; data curation, K.S.T. and I.D.C.; writing—original draft preparation, K.S.T., I.D.C. and P.N.T.; writing—review and editing, K.S.T., V.K. and B.Y.; supervision, K.S.T., V.K. and B.Y. All authors have read and agreed to the published version of the manuscript.

**Funding:** This research received no external funding.

**Data Availability Statement:** The datasets generated during and/or analyzed during the current study are available from the corresponding author on reasonable request.

**Acknowledgments:** The authors would like to thank K. Spyrou (Department of Materials Science and Engineering, University of Ioannina) for his support in the XPS measurements.

**Conflicts of Interest:** The authors declare no conflict of interest.

## References

- Vogt, E.T.C.; Weckhuysen, B.M. Fluid catalytic cracking: Recent developments on the grand old lady of zeolite catalysis. *Chem. Soc. Rev.* **2015**, *44*, 7342–7370.
- Gholami, Z.; Gholami, F.; Tišler, Z.; Tomas, M.; Vakili, M. A Review on Production of Light Olefins via Fluid Catalytic Cracking. *Energies* **2021**, *14*, 1089.
- Bai, P.; Etim, U.J.; Yan, Z.; Mintova, S.; Zhang, Z.; Zhong, Z.; Gao, X. Fluid catalytic cracking technology: Current status and recent discoveries on catalyst contamination. *Catal. Rev.* **2019**, *61*, 333–405.
- Etim, U.J.; Wu, P.; Bai, P.; Xing, W.; Ullah, R.; Subhan, F.; Yan, Z. Location and Surface Species of Fluid Catalytic Cracking Catalyst Contaminants: Implications for Alleviating Catalyst Deactivation. *Energy Fuels* **2016**, *30*, 10371–10382.
- Busca, G.; Riani, P.; Garbarino, G.; Ziembicki, G.; Gambino, L.; Montanari, E.; Millini, R. The state of nickel in spent Fluid Catalytic Cracking catalysts. *Appl. Catal. A Gen.* **2014**, *486*, 176–186.

6. Clough, M.; Pope, J.C.; Lin, L.T.X.; Komvokis, V.; Pan, S.S.; Yilmaz, B. Nanoporous materials forge a path forward to enable sustainable growth: Technology advancements in fluid catalytic cracking. *Microporous Mesoporous Mater.* **2017**, *254*, 45–58.
7. Corma, A.; Grande, M.S.; Iglesias, M.; del Pino, C.; Rojas, R.M. Nickel passivation on fluidised cracking catalysts with different antimony complexes. *Appl. Catal. A Gen.* **1992**, *85*, 61–71.
8. Petti, T.F.; Tomczak, D.; Pereira, C.J.; Cheng, W.-C. Investigation of nickel species on commercial FCC equilibrium catalysts—implications on catalyst performance and laboratory evaluation. *Appl. Catal. A Gen.* **1998**, *169*, 95–109.
9. Fu, H.; Chen, Y.; Liu, T.; Zhu, X.; Yang, Y.; Song, H. Research on Hazardous Waste Removal Management: Identification of the Hazardous Characteristics of Fluid Catalytic Cracking Spent Catalysts. *Molecules* **2021**, *26*, 2289.
10. Wang, Y.-J.; Wang, C.; Li, L.-L.; Chen, Y.; He, C.-H.; Zheng, L. Assessment of ecotoxicity of spent fluid catalytic cracking (FCC) refinery catalysts on Raphidocelis subcapitata and predictive models for toxicity. *Ecotoxicol. Environ. Saf.* **2021**, *222*, 112466.
11. Zhang, D.; Fang, S.; Zhang, H.; Liu, Z.; Zhang, Z.; Zhang, S. Utilization of Spent FCC Catalyst as Fine Aggregate in Non-sintered Brick: Alkali Activation and Environmental Risk Assessment. *Front. Chem.* **2021**, *9*, 240.
12. Ramezani, A.; Emami, S.M.; Nemat, S. Reuse of spent FCC catalyst, waste serpentine and kiln rollers waste for synthesis of cordierite and cordierite-mullite ceramics. *J. Hazard. Mater.* **2017**, *338*, 177–185.
13. Ferella, F.; D’Adamo, I.; Leone, S.; Innocenzi, V.; de Michelis, I.; Vegliò, F. Spent FCC E-Cat: Towards a Circular Approach in the Oil Refining Industry. *Sustainability* **2019**, *11*, 113.
14. Komvokis, V.; Keeley, C.; Challis, S. Bottoms up! Part One. *Hydrocarb. Eng.* **2013**, *18*, 64–66, 68, 70.
15. Pan, S.; Shackleford, A.; McGuire, R., Jr.; Smith, G.; Yilmaz, B. Creative Catalysis, Hydrocarbon Engineering (2015).
16. Bare, S.R.; Modica, F.S.; Ringwelski, A.Z. In situ Ni K-edge XANES study of the reducibility of Ni in f.c.c. catalysts. *J. Synchrotron Radiat.* **1999**, *6*, 436–438.
17. Stöcker, M.; Tangstad, E.; Aas, N.; Myrstad, T. Quantitative determination of Ni and V in FCC catalysts monitored by ESR spectroscopy. *Catal. Lett.* **2000**, *69*, 223–229.
18. Mitchell, B.R. Metal Contamination of Cracking Catalysts. 1. Synthetic Metals Deposition on Fresh Catalysts. *Ind. Eng. Chem. Prod. Res. Dev.* **1980**, *19*, 209–213.
19. Kallithrakas-Kontos, N.G.; Xarchoulakos, D.C.; Boultadaki, P.; Potiriadis, C.; Kehagia, K. Selective Membrane Complexation and Uranium Isotopes Analysis in Tap Water and Seawater Samples. *Anal. Chem.* **2018**, *90*, 4611–4615.
20. McCarthy, T.J.; Ngeyi, S.P.; Liao, J.H.; DeGroot, D.C.; Hogan, T.; Kannewurf, C.R.; Kanatzidis, M.G. Molten salt synthesis and properties of three new solid-state ternary bismuth chalcogenides, .beta.-CsBiS<sub>2</sub>, .gamma.-CsBiS<sub>2</sub>, and K<sub>2</sub>Bi<sub>8</sub>Se<sub>13</sub>. *Chem. Mater.* **1993**, *5*, 331–340.
21. Wallenstein, D.; Harding, R.H.; Nee, J.R.D.; Boock, L.T. Recent advances in the deactivation of FCC catalysts by cyclic propylene steaming (CPS) in the presence and absence of contaminant metals. *Appl. Catal. A Gen.* **2000**, *204*, 89–106.
22. Wallenstein, D.; Roberie, T.; Bruhin, T. Review on the deactivation of FCC catalysts by cyclic propylene steaming. *Catal. Today* **2007**, *127*, 54–69.
23. Bayraktar, O.; Kugler, E.L. Temperature-programmed reduction of metal-contaminated fluid catalytic cracking (FCC) catalysts. *Appl. Catal. A Gen.* **2004**, *260*, 125–132.
24. Psarras, A.C.; Iliopoulos, E.F.; Nalbandian, L.; Lappas, A.A.; Pouwels, C. Study of the accessibility effect on the irreversible deactivation of FCC catalysts from contaminant feed metals. *Catal. Today* **2007**, *127*, 44–53.
25. Vincz, C.; Rath, R.; Smith, G.M.; Yilmaz, B.; McGuire, R. Dendritic nickel porphyrin for mimicking deposition of contaminant nickel on FCC catalysts. *Appl. Catal. A Gen.* **2015**, *495*, 39–44.
26. Ferella, F.; Innocenzi, V.; Maggiore, F. Oil refining spent catalysts: A review of possible recycling technologies. *Resour. Conserv. Recycl.* **2016**, *108*, 10–20.
27. Zhang, C.C.; Shi, J.; Hartlaub, S.; Palamara, J.P.; Petrovic, I.; Yilmaz, B. In-situ diffuse reflective infrared Fourier transform spectroscopy (DRIFTS) study on Ni passivation in FCC catalysts from boron-based technology. *Catal. Commun.* **2021**, *150*, 106273.
28. Heracleous, E.; Lee, A.F.; Wilson, K.; Lemonidou, A.A. Investigation of Ni-based alumina-supported catalysts for the oxidative dehydrogenation of ethane to ethylene: Structural characterization and reactivity studies. *J. Catal.* **2005**, *231*, 159–171.
29. Samain, L.; Jaworski, A.; Edén, M.; Ladd, D.M.; Seo, D.-K.; Garcia-Garcia, F.J.; Häussermann, U. Structural analysis of highly porous  $\gamma$ -Al<sub>2</sub>O<sub>3</sub>. *J. Solid State Chem.* **2014**, *217*, 1–8.
30. Ragupathi, C.; Vijaya, J.J.; Surendhar, P.; Kennedy, L.J. Comparative investigation of nickel aluminate (NiAl<sub>2</sub>O<sub>4</sub>) nano and microstructures for the structural, optical and catalytic properties. *Polyhedron* **2014**, *72*, 1–7.
31. Garbarino, G.; Riani, P.; Infantes-Molina, A.; Rodríguez-Castellón, E.; Busca, G. On the detectability limits of nickel species on NiO/ $\gamma$ -Al<sub>2</sub>O<sub>3</sub> catalytic materials. *Appl. Catal. A Gen.* **2016**, *525*, 180–189.
32. Komvokis, V.G.; Karakoulia, S.; Iliopoulos, E.F.; Papapetrou, M.C.; Vasalos, I.A.; Lappas, A.A.; Triantafyllidis, K.S. Upgrading of Fischer-Tropsch synthesis bio-waxes via catalytic cracking: Effect of acidity, porosity and metal modification of zeolitic and mesoporous aluminosilicate catalysts. *Catal. Today* **2012**, *196*, 42–55.
33. Pu, X.; Liu, N.-w.; Shi, L. Acid properties and catalysis of USY zeolite with different extra-framework aluminum concentration. *Microporous Mesoporous Mater.* **2015**, *201*, 17–23.
34. Nishimura, Y. Development of Catalytic Cracking Process and Catalysts. *Adv. Porous Mater.* **2017**, *5*, 17–25.
35. Scherzer, J. Octane-Enhancing, Zeolitic FCC Catalysts: Scientific and Technical Aspects. *Catal. Rev.* **1989**, *31*, 215–354.
36. Blay, V.; Louis, B.; Miravalles, R.; Yokoi, T.; Peccatiello, K.A.; Clough, M.; Yilmaz, B. Engineering Zeolites for Catalytic Cracking to Light Olefins. *ACS Catal.* **2017**, *7*, 6542–6566.

37. Farshi, A.; Abri, H.R. The Addition of ZSM-5 to a Fluid Catalytic Cracking Catalyst for Increasing Olefins in Fluid Catalytic Cracking Light Gas. *Pet. Sci. Technol.* **2012**, *30*, 1285–1295.
38. Costa, T.M.H.; Gallas, M.R.; Benvenutti, E.V.; da Jornada, J.A.H. Study of Nanocrystalline  $\gamma$ -Al<sub>2</sub>O<sub>3</sub> Produced by High-Pressure Compaction. *J. Phys. Chem. B* **1999**, *103*, 4278–4284.
39. Darmakkolla, S.R.; Tran, H.; Gupta, A.; Rananavare, S.B. A method to derivatize surface silanol groups to Si-alkyl groups in carbon-doped silicon oxides. *RSC Adv.* **2016**, *6*, 93219–93230.
40. El-Kemary, M.; Nagy, N.; El-Mehasseb, I. Nickel oxide nanoparticles: Synthesis and spectral studies of interactions with glucose. *Mater. Sci. Semicond. Process.* **2013**, *16*, 1747–1752.
41. Li, J.; Ren, Y.; Yue, B.; He, H. Ni/Al<sub>2</sub>O<sub>3</sub> catalysts derived from spinel NiAl<sub>2</sub>O<sub>4</sub> for low-temperature hydrogenation of maleic anhydride to succinic anhydride. *Chin. J. Catal.* **2017**, *38*, 1166–1173.
42. Domingo, A.; Rodríguez-Fortea, A.; Swart, M.; de Graaf, C.; Broer, R. Ab initio absorption spectrum of NiO combining molecular dynamics with the embedded cluster approach in a discrete reaction field. *Phys. Rev. B* **2012**, *85*, 155143.
43. Huang, W.; Ding, S.; Chen, Y.; Hao, W.; Lai, X.; Peng, J.; Tu, J.; Cao, Y.; Li, X. 3D NiO hollow sphere/reduced graphene oxide composite for high-performance glucose biosensor. *Sci. Rep.* **2017**, *7*, 5220.
44. Mrabet, C.; Amor, M.B.; Boukhachem, A.; Amlouk, M.; Manoubi, T. Physical properties of La-doped NiO sprayed thin films for optoelectronic and sensor applications. *Ceram. Int.* **2016**, *42*, 5963–5978.
45. Wang, W.; Liu, Y.; Xu, C.; Zheng, C.; Wang, G. Synthesis of NiO nanorods by a novel simple precursor thermal decomposition approach. *Chem. Phys. Lett.* **2002**, *362*, 119–122.
46. Choi, H.C.; Jung, Y.M.; Kim, S.B. Size effects in the Raman spectra of TiO<sub>2</sub> nanoparticles. *Vib. Spectrosc.* **2005**, *37*, 33–38.
47. Laguna-Bercero, M.A.; Sanjuán, M.L.; Merino, R.I. Raman spectroscopic study of cation disorder in poly- and single crystals of the nickel aluminate spinel. *J. Physics. Condens. Matter* **2007**, *19*, 186217.
48. Lubas, M.; Jasinski, J.J.; Sitarz, M.; Kurpaska, L.; Podsiad, P.; Jasinski, J. Raman spectroscopy of TiO<sub>2</sub> thin films formed by hybrid treatment for biomedical applications. *Spectrochim. Acta Part A: Mol. Biomol. Spectrosc.* **2014**, *133*, 867–871.
49. Jiménez-González, C.; Boukha, Z.; de Rivas, B.; Delgado, J.J.; Cauqui, M.Á.; González-Velasco, J.R.; Gutiérrez-Ortíz, J.I.; López-Fonseca, R. Structural characterisation of Ni/alumina reforming catalysts activated at high temperatures. *Appl. Catal. A Gen.* **2013**, *466*, 9–20.
50. Kitakatsu, N.; Maurice, V.; Hinnen, C.; Marcus, P. Surface hydroxylation and local structure of NiO thin films formed on Ni(111). *Surf. Sci.* **1998**, *407*, 36–58.
51. Natile, M.M.; Glisenti, A. Surface Reactivity of NiO: Interaction with Methanol. *Chem. Mater.* **2002**, *14*, 4895–4903.
52. Riman, D.; Spyrou, K.; Karantzalis, A.E.; Hrbac, J.; Prodromidis, M.I. Glucose sensing on graphite screen-printed electrode modified by sparking of copper nickel alloys. *Talanta* **2017**, *165*, 466–473.
53. McIntyre, N.S.; Cook, M.G. X-ray photoelectron studies on some oxides and hydroxides of cobalt, nickel, and copper. *Anal. Chem.* **1975**, *47*, 2208–2213.
54. Kugler, E.L.; Leta, D.P. Nickel and vanadium on equilibrium cracking catalysts by imaging secondary ion mass spectrometry. *J. Catal.* **1988**, *109*, 387–395.
55. Lappas, A.A.; Nalbandian, L.; Iatridis, D.K.; Voutetakis, S.S.; Vasalos, I.A. Effect of metals poisoning on FCC products yields: Studies in an FCC short contact time pilot plant unit. *Catal. Today* **2001**, *65*, 233–240.
56. Pan, S.S.; Lin, L.T.X.; Komvokis, V.; Spann, A.; Clough, M.; Yilmaz, B. Nanomaterials Fueling the World. *Nanomaterials for Sustainable Energy*; American Chemical Society: Washington, DC, USA, 2015; pp. 3–18.
57. Cheng, W.C.; Juskelis, M.V.; Suárez, W. Reducibility of metals on fluid cracking catalyst. *Appl. Catal. A Gen.* **1993**, *103*, 87–103.

**Disclaimer/Publisher's Note:** The statements, opinions and data contained in all publications are solely those of the individual author(s) and contributor(s) and not of MDPI and/or the editor(s). MDPI and/or the editor(s) disclaim responsibility for any injury to people or property resulting from any ideas, methods, instructions or products referred to in the content.